# Experimental and numerical analysis of the bi-stable turbulent wake of a rectangular flat-backed bluff body

Yajun Fan(范亚军),[1,2] Chao Xia(夏超),[1,2,a)] Shijun Chu(储世俊),[1,2] Zhigang Yang(杨志刚),[1,2,3] and Olivier Cadot[4]

[1)] *School of Automotive Studies, Tongji University, Shanghai 201804, China*

[2)] *Shanghai Automotive Wind Tunnel Center, Tongji University, Shanghai 201804, China*

[3)] *Beijing Aeronautical Science  Technology Research Institute, Beijing 102211, China*

[4)] *School of Engineering, University of Liverpool, Liverpool L69 3GH, UK*

(Dated: 19 September 2020)

The wake dynamics of a rectangular flat-backed bluff body is studied using both wind tunnel experiment and Improved Delayed Detached Eddy Simulation (IDDES) at Re $= 9.2 \times 10^4$. Both approaches are systematically investigated in order to provide a quantitative comparison. Wake barycentre deficit and base pressure gradients dynamics are first investigated to characterize the wake states. Secondly, the known global dynamics such as long-term bi-stability, vortex shedding and wake pumping are analysed using proper orthogonal decomposition. It is found that the wake dynamics is globally well captured by the IDDES, but with a more intense activity due to the absence of the fore-body separations observed in the experiment. The coupling of these global dynamics is explored by utilizing low-order modelling in cross-planes and elaborating the evolution of the three-dimensional instantaneous wake flow from IDDES. The shedding of a large-scale hairpin vortex from the horizontal shear layer is closely associated with the pumping motion during wake switchings or switching attempts. A concept model is proposed for 3D bi-stable wake topology, which attempts to elucidate both asymmetric and symmetric wake configurations.

[a)] Electronic mail: chao.xia@tongji.edu.cn

## I. INTRODUCTION

The wake topology is fundamental to a ground vehicle drag. Most ground vehicles (sport utility vehicle, multi-purpose vehicle, truck and bus, etc) are three-dimensional (3D) bluff bodies with blunt rear geometry responsible for a massive flow separation leading to a complex 3D turbulent wake. For a better understanding of the wake dynamics aiming at improving their aerodynamic performances, simplified models such as the Ahmed body[1] have been extensively studied over the last decades. Previous studies[2] found three major flow structures in the wake of this body: a separation bubble over the slanted surface or rear window, one pair of counter-rotating longitudinal or C-pillar vortices originating from the two side edges of the rear window, and a recirculation torus behind the vertical base. These flow structures and their interaction depend on the slant angle of the rear window. Most researches have focused on the 25◦ or 30◦ slanted geometry, mainly for the interest in finely characterizing this complex 3D configuration[3–5].

However, in recent years, more and more researches have been carried out on the wake behind a square back Ahmed body, characterized by a rectangular flat-backed bluff body, since the seminal work of Grandemange *et al.*[6] who documented and characterized a bi-stable flow behavior on a 1/4 scale model square back Ahmed body. The bi-stability is a long time scale of the order of $1000H/U_\infty$ (where $U_\infty$ is free-stream velocity, $H$ the height of the model) flow phenomenon. It represents the random shift of the recirculation region between two reflectional symmetry-breaking (RSB) positions which is mutually symmetric with respect to the vertical central plane, leading to a statistically symmetric wake. Complementary research[7] was performed by the same authors, who find out that the occurrence of the bi-stability is determined by the ground clearance and the aspect ratios. In addition, high degrees of asymmetry are reported in experiments[6] and numerical simulations[8] despite the symmetry of the set-up. Studies[9,10] of the square back Ahmed body at low Reynolds numbers suggest that the bi-stable behavior appears after a pitchfork bifurcation in the laminar regime. More researches[11,12] suggest that this phenomenon is independent of the Reynolds number (Re), at least for Re up to $2.5 \times 10^6$ which corresponds to the scale of a real vehicle in road conditions.

Similar bi-stable characteristics have been observed in various turbulent wake such as the separated flow over the in-notch region of a Notchback MIRA model[13], a three-dimensional double backward facing step[14] and a three-dimensional axisymmetric body[15]. In contrast to the wake generated by a rectilinear body, however, for an axisymmetric body, the wake does not switch between two symmetry-breaking states but moves between an infinite number of states depending on the azimuthal angle of the shedding[16]. Bonnavion *et al.*[17]. investigated the real minivans' wake and also observed the bi-stability in the vertical direction. The sequence of the RSB mode was initially thought to behave like a stationary Markov chain[6], however the nonlinear dynamic analysis from Varon *et al.*[18] suggest that the low frequencies dynamics associated with large-scale structures can be considered as a weak chaotic strange attractor.

The numerical simulation of bi-stable wake is a difficult task, due to its very long timescale. Lucas *et al.*[8] conducted a numerical simulation of the turbulent flow over the square backed Ahmed body by using a lattice Boltzmann solver. However, the succession of the two mirror asymmetric modes were not observed during the finite time of the simulation. Zhang *et al.*[19] conducted the numerical simulation for the flow past a generic ship by using the PANS and LES methods, and the result shows that the occurrence of the two stable states is dependent on the spatial resolution. The research work conducted by Rao *et al.*[20] also indicated that the different numerical scheme plays a critical role in predicting the bi-stable behavior in the near wake of a ground transportation system. However, all these works only obtained one state of bi-stable behavior in a single case. Recently, Dalla Longa *et al.*[21] simulated the bi-modal behavior of the turbulent flow past a simplified lorry and Ahmed body by using wall-resolved large eddy simulations, and proposed that the large hairpin vortex structure, which was shed from the longest edge of the base, appeared to be responsible for the triggering bi-stable switches.

After the bi-stable behavior in the wake behind 3D bluff bodies was observed, more studies have begun to focus on the evolution of different unsteady flow structures. It is widely known that there are three different unsteady flow modes in the wake over the flat-backed 3D bluff bodies. Except for the long time-scale bi-stable behavior described above, previous studies[6,11,22,23] also observed a shorter time-scale unsteady flow structure which was attributed to weak coherent oscillations of the wake in the vertical and lateral directions, associated with the interaction of top-bottom and lateral shear layers. A lower-frequency mode was found by Khalighi *et al.*[24,25] for the Ahmed body and by Duell and George[26] on a bluff body similar to the one from Ahmed, but with a square section. This mode is usually interpreted as pumping of the whole recirculation bubble[27]. In order to identify the causal relationship between the different dynamic modes in the wake, Pavia *et al.*[28] and Perry *et al.*[29] carried out an extensive experimental campaign on the bi-stable behavior of the Windsor body, and proposed a new structure for each RSB state by applying proper orthogonal decomposition. The analysis of the low-order phase-averaged velocity field indicated that the bi-stable mode is the result of the interaction between the two horizontal shear layers. Recently, Haffner *et al.*[30] studied experimentally the bi-stable switching occurring between two RSB states and proposed that the interaction of the recirculating flow triggering the shear layer and the roll-up of the shear layer leading to engulfed flow promoting and feeding the recirculating flow is the key process.

To the author's knowledge, the link between the long-term bi-stable and the higher frequency oscillation modes has not been fully understood in the literature so far. One may ask the following questions: how do these unsteady wake modes couple with each other? Moreover, what is happening during the transient bi-stable wake switching? As mentioned, only few reported numerical simulations are performed on this bi-stable wake due to its very long timescale and sensitivity to grid resolution. Hence, there are still open questions about 3D unsteady wake topology and its vortex dynamics.

The aim of the work presented in this paper is twofold: to make a detailed comparison of the ability of the experiment measurement and the Improved Delayed Detached Eddy Simulation (IDDES) to capture the unsteady wake, especially the long time bi-stable behavior, and to further investigate the unstable 3D wake behind the square back Ahmed body. The proper orthogonal decomposition, spectral analysis and low-order modelling are applied to the velocity data set to identify the predominant flow structure and the causal relationship between different dynamic modes. The final goal of this research is to clarify the 3D unsteady wake topology, the coupling between different vortex structures and the triggering mechanism for the bi-stable switching.

The article is organized as follows. In Sec. II, the research methodologies are presented in detail. Then, Sec. III is devoted to the comparison between the experiment results and simulation results with a focus on the global wake dynamics. The interaction between different vortex structures are studied in Sec. IV. Eventually, concluding remarks are presented in Sec. V.

## II. RESEARCH METHODOLOGIES

### A. Experimental set up and measurements technique

The experimental campaigns were conducted in a three-quarters open-jet close-loop low speed wind tunnel, with a noozle section of 432 mm wide × 288 mm high entering a plenum of size 1185 mm×1520 mm×810 mm, as shown in Fig. 1(a,b). The maximum wind speed is about

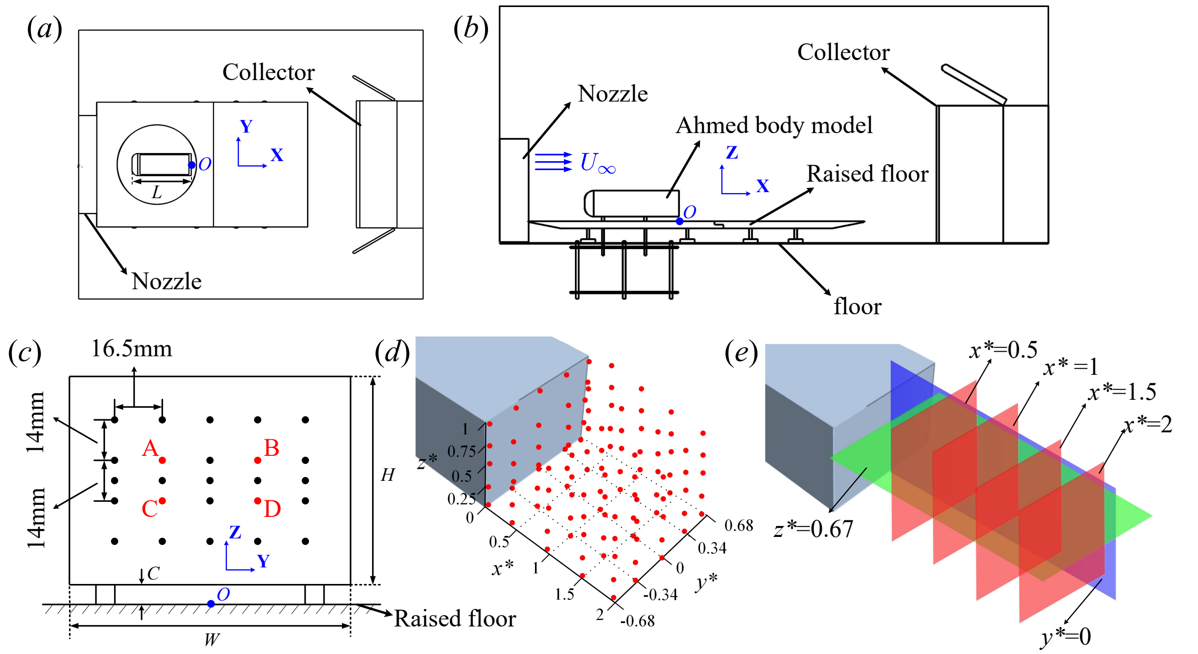


FIG. 1. Experimental apparatus: (a) top view and (b) side view of the plenum; (c) Positions of the pressure taps; (d) Positions of hot-wire probe; (e) The 2D PIV sampling planes.

49 m/s, and the axial static pressure gradient is less than 0.005 Pa/m. The turbulent intensity at the exit of the nozzle is less than 0.5%. Fig. 1(a) shows the schematic of the experimental setup and the definition of the coordinate system. The 1/4 scaled square-back Ahmed body (length $L = 261$ mm, height $H = 72$ mm, width $W = 97.25$ mm, ground clearance 12.5 mm) is placed over a raised floor which ensures constant flow conditions, as shown in Fig. 1(a). The diameter of the support is 8 mm. When the model is not in the test section, the ground boundary layer thickness based on 99% of the free-stream velocity at $x = -L$, i.e. 140 mm downstream of the leading edge of the raised floor, is $\delta_{99} = 4.6$ mm with a precision of 0.1 mm. The blockage ratio is less than 7%.The free-stream velocity is $U_\infty = 20$ m/s.

The height of the body $H$ and the main incoming velocity $U_\infty$ are chosen respectively as length and velocity scaling units. For the remainder of the paper any quantity $a$ with superscript $a^*$ is expressed in these non-dimensional units. For instance, non-dimensional time and is defined as $t^* = tU_\infty/H$. The non-dimensional coordinates are defined as $x^* = x/H$, $y^* = y/H$ and $z^* = z/H$. The corresponding Reynolds numbers is $\mathrm{Re} = U_\infty H/\nu = 9.2 \times 10^4$, with $\nu$ being the air kinematic viscosity. Non dimensional frequencies are expressed using the Strouhal number defined as $St = fH/U_\infty$.

The base (i.e. the flat surface at the back of the body) is equipped with 25 pressure taps, as shown in Fig. 1(c). The pressure is obtained using a 24-port pressure scanner with an accuracy of ±3 Pa. The vinyl tubes with a length of 550 mm go through the four supports of the model so that, apart from the supports, nothing disturbs the underbody flow. The pressure scanner takes 50 pressure samples per second, the total sampling time is 600 s. Pressure coefficient is defined as follows:

$$c_p = \frac{p - p_\infty}{\frac{1}{2}\,\rho\, U_\infty^2}, \tag{1}$$

where $p$ is pressure of the orifices, $p_\infty$ is static pressure of the onset flow and $\rho$ the air density.The instantaneous base suction coefficient $c_b$ is assessed from the 21 pressure taps of the base (taps in Fig. 1(b) except those close to the corners):

$$c_b = -\iint_{H\times W} c_p ds \approx -\frac{1}{21}\sum_{i=1}^{21} c_p(y_i^*, z_i^*). \tag{2}$$

Following the similar experimental procedure as Grandemange *et al.*[6], four of the pressure taps are used to compute the base pressure gradient which is representative of the instantaneous configuration of the wake. The dimensionless horizontal $g_y^*$ and vertical $g_z^*$ pressure gradient coefficient components are computed as follows using the pressure taps marked A, B, C and D in Fig. 1(c):

$$g_y^* = \frac{1}{2}\times\left[\frac{(c_{p\mathrm{B}}+c_{p\mathrm{D}})-(c_{p\mathrm{A}}+c_{p\mathrm{C}})}{y_B^* - y_A^*}\right] \tag{3}$$

and:

$$g_z^* = \frac{1}{2}\times\left[\frac{(c_{p\mathrm{A}}+c_{p\mathrm{B}})-(c_{p\mathrm{C}}+c_{p\mathrm{D}})}{z_A^* - z_C^*}\right] \tag{4}$$

Two single-component hot wires (Dantec 55P01) were used to measure streamwise fluctuating velocity $u$ to detect the predominant frequencies in the wake flow. The hot wires were traversed along the streamwise direction ($x^*$ = 0, 0.5, 1, 1.5, 2 at $y^*$ = 0, ±0.34, ±0.68 and $z^*$ = 0, 0.25, 0.5, 0.75, 1), as shown in Fig. 1(c), obtaining velocity signals at a total of 116 measuring points. The hot wires were operated on a constant-temperature circuit (Dantec Streamline) at an over heat ratio of 1.4. The signals from the wires were digitized at a sampling frequency of 2.0 kHz using a 16-bit analogue-to-digital converter. The sampling duration was 60 s, producing a total of $1.2\times10^6$ data for each record. The fast Fourier transform (FFT) algorithm was employed to calculate the power spectral density function.

A Particle Image Velocity (PIV) system from TSI was used to measure the two dimensional velocity field in the wake. The flow was seeded by smoke generated from corn oil, with particles of approximately 1 to 5 $\mu$m in diameter. Flow illumination was provided by two Vlite-500 pulse laser sources of 532 nm wavelength, each with a maximum energy output of 500 mJ per pulse. Each laser pulse lasted for 0.01 $\mu$s. Particle images were taken using a charge-coupled device (CCD) camera (PowerviewPlus type 29M, double frames, 6600 pixels $\times$ 4400 pixels). Synchronization between image capturing and flow illumination was controlled by the 610036 Laser-Pulse Synchronizer. Conventional notations for the velocity field $\vec{u}(x,y,z)$ is used denoting by $u$, $v$ and $w$ its $x$, $y$ and $z$ component respectively. Reynolds decomposition is denoted as $u = \mathrm{U} + u'$ for the $x$ component with a upper case letter for the temporal averaging $U = \langle u \rangle$.

The two-dimensional (2D) PIV measurements were performed in four cross-flow planes $x^*$ = 0.5, 1, 1.5, 2 and horizontal mid-plane $z^* = 0.67$ and vertical mid-plane $y^* = 0$, as shown in Fig. 1(e). The image magnifications in the cross-flow, horizontal and vertical planes are 87, 70 and 72 $\mu$m/pixel respectively. The time interval between two successive pulses was 10 $\mu$s for measurements in horizontal and vertical planes. In the cross-flow planes, the CCD camera was placed on the ground inside the wind tunnel, about 10$H$ downstream from the model to minimize any possible disturbance to the wake flow. Since the main stream is normal to the cross-flow plane, the out-of-plane component of velocity is relatively large compared to the measurements in the two other planes, that is, the tracing particles could cross the light sheet given a large time interval between two successive images used in determining velocity vectors ($v$ and $w$), thus resulting in poor correlation[31,32]. Thus, the time interval was set to 5 $\mu$s for the measurement in the cross-flow planes, which was found to produce satisfactory results.

In the cross-correlation algorithm, the interrogation area was chosen to be 48$\times$48 pixels corresponding to 3.8$\times$3.8 mm in cross-flow plane measurements and 3.4$\times$3.4 mm in the horizontal and vertical planes with 50% overlap in both directions. The sampling frequency of the PIV system was 1.25 Hz. A total of 1000 pairs of PIV images were captured to calculate the mean velocity and to perform Proper Orthogonal Decomposition (POD) analysis in each plane.

### B. Numerical simulation set-up

The size of the computational domain is 40$H$ (length) $\times$ 9.4$H$ (width) $\times$ 5$H$ (height) and the details are shown in Fig. 2. The size of the square back Ahmed body is the same as the experimental model, except that the diameter of the support is 7.5 mm. These dimensions give a blockage ratio of 2.86%. The boundary conditions are specified as following: velocity inlet

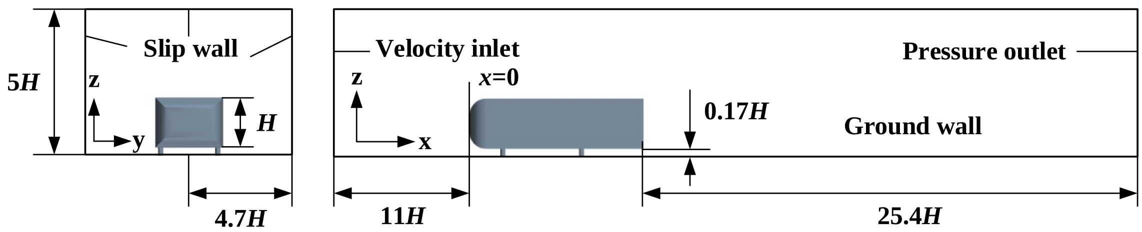


FIG. 2. Computational domain and boundary conditions.

for the inlet; pressure outlet for the outlet, non-slip wall condition for the Ahmed body and the stationary ground; symmetry for the rest boundaries. The numerical simulation was performed with the commercial unstructured finite-volume solver STAR-CCM+, which is a mature code that has been extensively verified and validated on the flow around bluff bodies[33–35]. The computation is based on the three-dimensional incompressible Navier–Stokes equations and IDDES. The time-dependent IDDES (based on SST model)[36] used in this paper is a hybrid RANS-LES model, which combines the advantages of the delayed detached-eddy simulation (DDES) and the wall-modelled large eddy simulation (WMLES). The DDES provides shielding against grid-induced separation (GIS) caused by the grid refinement beyond the limit of the modelled stress depletion (MSD)[37]. The WMLES model is designed to reduce the Reynolds number dependency and to allow the LES simulation of wall boundary layers at much higher Reynolds numbers than standard LES models[38]. Besides, in IDDES a new sub-grid length-scale is defined in Eq. (5) that includes explicit wall-distance dependence, different from the usual LES and DES practice which involves only the grid-spacing.

$$\Delta = \mathbf{min}\{\mathbf{max}[C_w d_w, C_w h_{\max}, h_{wn}], h_{\max}\}, \tag{5}$$

where $d_w$ is the distance to the wall, $h_{wn}$ is the grid step in the wall-normal direction and $C_w$ is an empirical constant that is equal to 0.15 based on a wall-resolved LES of channel flow. $h_{\max}$ is defined as the largest local grid spacing:

$$h_{\max} = \mathbf{max}\{h_x, h_y, h_z\}. \tag{6}$$

The complete formulation in IDDES is relatively complex and has been implemented by Shur *et al.*[38]. The pressure-velocity coupling algorithms is PISO (Pressure Implicit with Splitting of operators). The convective Courant-Friedrichs-Lewy (CFL) time-step control model is applied,

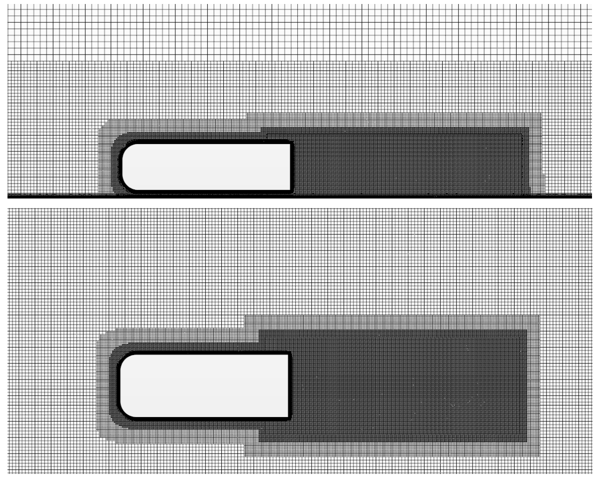

FIG. 3. Medium grids distribution in symmetry plane $y^* = 0$ and $z^* = 0.67$.

TABLE I. Spatial resolution for coarse, medium and fine grids.

| Grids | $y^+ = \Delta n u_\tau/\nu$ | $z^+ = \Delta s u_\tau/\nu$ | $x^+ = \Delta l u_\tau/\nu$ | Total number |
|---|---|---|---|---|
| Coarse | 1 | 90 | 90 | 6.0 million |
| Medium | 1 | 45 | 45 | 10.5 million |
| Fine | 1 | 36 | 36 | 22.2 million |

which automatically adjusts the time-step so that the actual CFL number approaches either specified maxima (5) or specified means (0.5), whichever yield the minimum time-step. To discretize the convective terms of the momentum equations, a hybrid MUSCL (Monotonic Upwind Scheme for Conservation Laws) third-order/central-differencing scheme was used to switch between a MUSCL third-order scheme and a second order upwind scheme, while a second order upwind scheme was used for the turbulent quantities. The Algebraic Multi-grid (AMG) linear solver was employed by using a Flex cycle for the momentum equations and the turbulent quantities. In addition, a synthetic eddy method (SEM) was specified in the velocity inlet, which is a simple, yet effective, approach for generating the instantaneous velocity field that is required for LES and DES. The SEM, proposed by Jarrin *et al.*[39], retains the conceptual basis of the vortex method, but is more flexible and virtually mesh-independent.

The topology of the computational grid is trimmer, which contains prism layers at the wall boundaries and a perfect hexahedral grid in the rest of the domain, and the prism layers are connected to the hexahedral grids by trimming them. A sensitivity study is performed on three sets

TABLE II. Drag coefficient $C_d$, base suction coefficient $C_b$ and length of the recirculation bubble $L_r$ for the 3 grids in Table I compared to experiments of identical geometry.

| | Approach | Re | $C_d$ | $C_b$ | $L_r^*$ |
|---|---|---|---|---|---|
| Coarse | CFD | $9.2 \times 10^4$ | 0.310 | 0.191 | 1.76 |
| Medium | CFD | $9.2 \times 10^4$ | 0.315 | 0.203 | 1.51 |
| Fine | CFD | $9.2 \times 10^4$ | 0.318 | 0.206 | 1.49 |
| Experiment | Exp | $9.2 \times 10^4$ | ... | 0.178 | 1.43 |
| Grandemange *et al.*[6] | Exp | $9.2 \times 10^4$ | 0.274 | 0.185 | 1.47 |

of grids with different numbers of cells: coarse, medium and fine grids consisting of 6.0 million, 10.5 million and 22.2 million cells, respectively. The maximum spatial resolutions of the model surface-cells expressed in the wall units are shown for the three sets of grids in Table I in the revised paper, where $u_\tau$ is the friction velocity, $\Delta n$ is the distance between the first node and the model surface in the wall normal direction, $\Delta l$ is the cell width in the streamwise direction and $\Delta s$ is the cell width in the spanwise direction. All grids are symmetric around the body to avoid introducing asymmetry in the flow. Fig. 3 shows the medium grids distribution with $y^+ \approx 1$, $z^+ \approx 45$ and $x^+ \approx 45$. The mesh in the wake region is refined up to 1.25 mm corresponding to $z^+(x^+) \approx 45$ and outside the wake region the mesh size increases by a factor of two with the maximum mesh size equaling to 10mm on the boundaries of the domain.

### C. Choice of the grid in the numerical simulation

The numerical simulation is designed to reproduce the experimental measurements obtained in this paper and those of Grandemange *et al.*[6]. In order to verify the effect of grid quality on the simulation results, three different spatial resolutions as defined in Table I were used. As shown in Table II, the differences between the medium and the fine grid are very small for either the mean drag coefficient $C_d$, the mean base suction coefficient $C_b$ or the length of the recirculation bubble $L_r^*$ (defined by the furthest downstream distance from the base having negative mean streamwise velocity in the vertical $y^* = 0$ plane). The medium grid has therefore been chosen as a good compromise to provide the numerical result of the paper.

The main difference from the mean flow obtained by Grandemange *et al.*[6] is the absence of flow separations at the four sides of the fore-body as shown in Fig. 4(a,b) that would have been unambiguously located by unsteady reattachments of large Reynolds stresses[6] on the flat surfaces for $x^* < -2$. The mean pressure distribution around the fore-body (Fig. 4c,d) for our experiment is very close to that of Grandemange *et al.*[6] which suggests similar fore-body separations. On the other hand, the computed pressure distribution is drastically different and produces at first glance a lower fore-body pressure drag than in the experiments. The incapacity of the IDDES to capture these separation bubbles modifies the boundary layers development all over the body until the after-body separations leading to a larger base suction $C_b$ as can be seen in Table II. However, this suction increase alone cannot explains the drag discrepancy between the values 0.274 of Grandemange *et al.*[6] and 0.318 of the simulation. Therefore, the drag contribution of the fore-body for the simulation must increase as a consequence of the absence of fore-body separations likely due to much higher friction drag since pressure drag is lower at the front. Nevertheless, it can be found large discrepancies in the literature[6,11] and the drag coefficients obtained by the IDDES fall within this range. The large discrepancies could actually be ascribed to the fore-body separation, that is sensitive to the Reynolds number and the free stream properties of the wind tunnel. Finally, a total duration of $T$ =20.2 s was carried out (i.e. $T^* = 5612$), and the bi-stable behavior has been successfully captured by the medium grid. The total computational time needed on 112 cores was about 1200 h. In the following sections, a systematic comparison will be made between the simulation and the experiment including conditional averaging and POD modes.

## III. COMPARISON BETWEEN EXPERIMENT AND SIMULATION

### A. Long-time dynamics of the wake

The bi-stable behavior is first captured through the barycenter of the wake momentum deficit in the $z^* = 0.67$ plane defined as:

$$y_w^* = \frac{\int y^*(1-u^*)ds}{\int(1-u^*)ds}, \tag{7}$$

$$x_w^* = \frac{\int x^*(1-u^*)ds}{\int(1-u^*)ds}, \tag{8}$$

with a domain of integration limited to $u^* < 1$. Fig. 5(a) shows the time evolution of $y_w^*$ obtained from 1000 PIV snapshots sampled at 1.25Hz during 800s. This distribution clearly highlights two distinct wake positions in the $y-$direction centred on $y_w^* = \pm 0.05$, which is in accordance with the

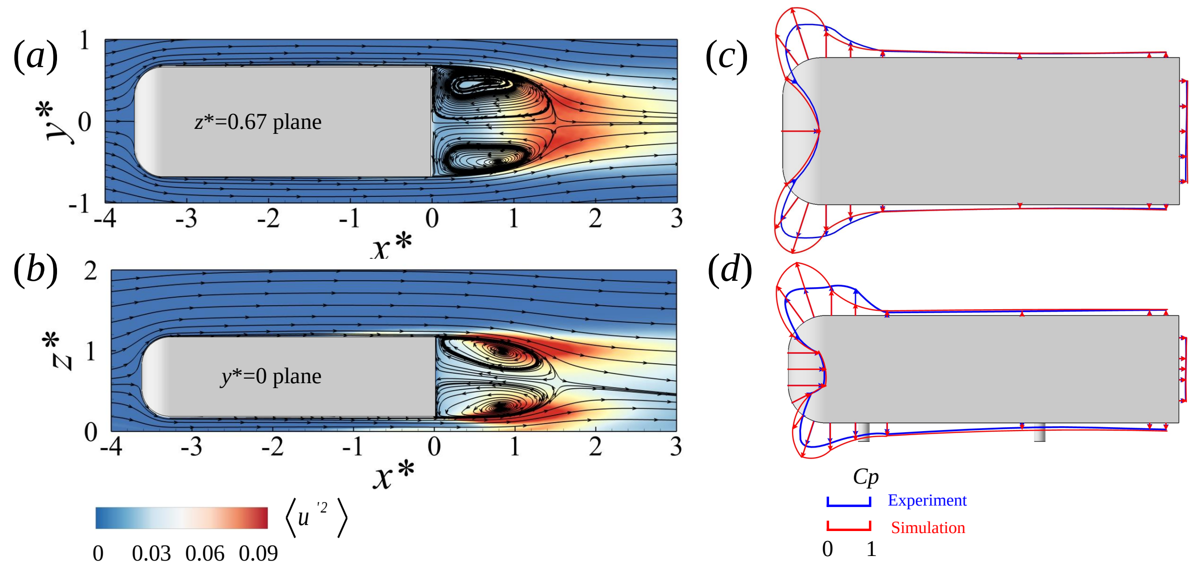


FIG. 4. Contours of Reynolds stresses $< u'^2 >$ superimposed to the mean flow streamlines in the y*=0 (a) and z*=0.67 (b) planes for the simulation with the medium grid. Mean pressure coefficient distribution around the body for the simulation (red) and the experiment (blue) in the y*=0 (c) and z*=0.67 (d) planes.

previous result from Grandemange *et al.*[6].The states are denoted by P for the one associated with a positive value of $y_w^*$ and N for the one with a negative value. Switching between the P and N states are more obvious in the zoom shown in the inset of Fig. 5(a) albeit the low time resolution of the PIV. Both stable positions are quantitatively captured by the IDDES numerical simulation as can be clearly seen in Fig. 5(b) providing only 2 switching but with a good time resolution. The time-scale of the switching dynamics is of order $t^* \sim 1000$ in agreement to the literature published on this bi-stable dynamics.

In addition to the barycenter of momentum deficit, the base pressure gradient is considered as an indicator of the bi-stability phenomenon. The advantage is the better time resolution for the experiment with a sampling at 50 Hz instead of the 1.25 Hz of the PIV. The time evolutions of the 2 components of the pressure gradient coefficient defined in Eqs. (3,4) are plotted in Fig. 6 for both the experiment (Fig. 6 (a,d)) and the simulation (Fig. 6 (b,e)). Despite the longer duration of the experimental time history, a very good agreement is again observed. It can be seen that accordingly to the above definition of the P and N states, the P (resp. N) state corresponds to a positive (resp. negative) pressure gradient. The larger fluctuations about each state for the simulation is explained by the absence of filtering whilst the tubing and the scanner introduce a

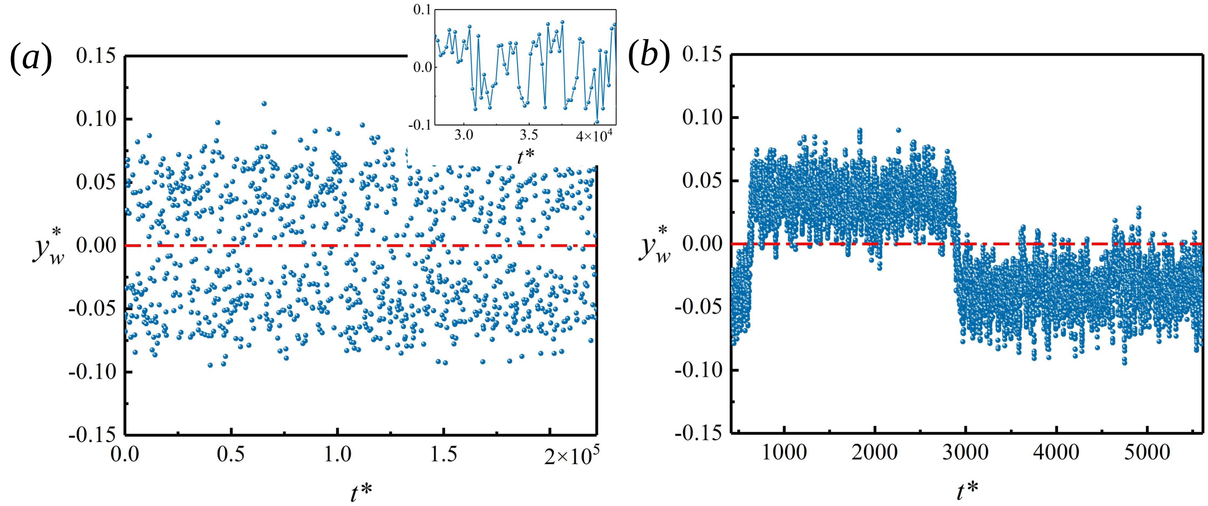


FIG. 5. Time evolution of the barycenter of momentum deficit in the $z^* = 0.67$ plane in the $y$-direction: (a) experiment; (b) simulation.

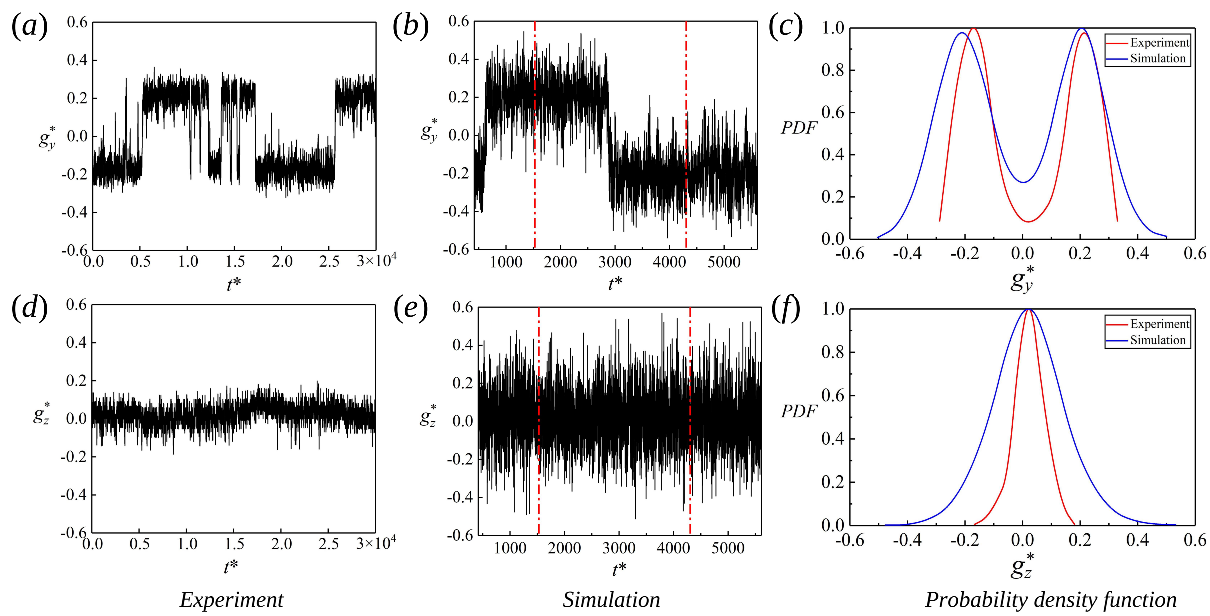


FIG. 6. Time evolution of the base pressure gradient components $g_y^*$ (a,b) and $g_z^*$ (d,e) for the experiment (a,d) and the simulation (b,e) and their probability density functions (c,f) normalized by the maximum.

low-pass filtering. Probability density functions (PDF) are performed on the largest statistical set of the time history such that states P and N are equiprobable. The set corresponds to the full duration for the experiment and to the data within the two vertical red dashed lines in Fig. 6(b,e)

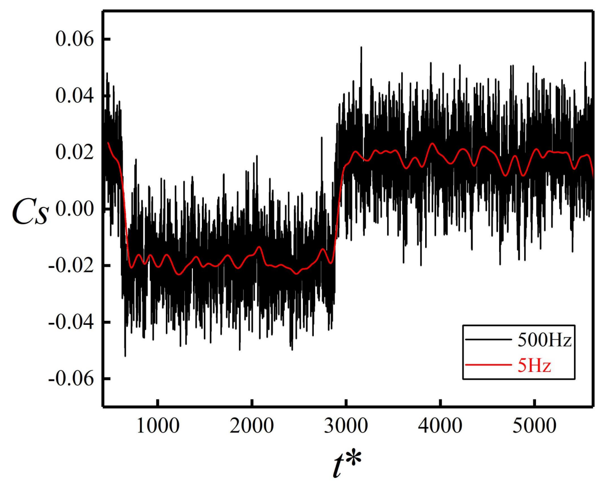


FIG. 7. Time evolution of the side force signals from simulation.

for the simulation. The two most probable horizontal gradients are opposite for the simulation in agreement to the reflectional symmetry of the geometry while the experimental PDF presents a small shift of approximately 0.03. The shift could be caused by cumulative errors of the model installation and pressure scanner calibration. Despite this small bias, the gradient components in the *y*-direction of both states are quantitatively retrieved by the computation with values of $\pm 0.2$. These are larger than those obtained by Grandemange *et al.*[6,7] who obtained $\pm 0.17$. The difference might be attributed on the way the gradient is computed. The gradient components in the *z*-direction $g_z^*$ are kept stable near a slightly positive value of 0.02 both for the experiment (Fig. 6d) and simulation (Fig. 6e), and their probability density distribution (Fig. 6f) are characterized by a single peak, which implies that the bi-stable behavior only occurs in the horizontal direction as expected from the parametric shape study[7]. The presence of the ground thus produces opposite effects in the present study that remains however an order of magnitude smaller than the horizontal asymmetry produced by the instability.

Fig. 7 shows the consequence of the bistable wake behavior on the instantaneous side force coefficient computed with the numerical simulation and the corresponding 5 Hz filtered result (red line). The most probable value of $C_s$ for the two asymmetric states are clearly distinguishable and correspond to -0.02 for the P state and +0.02 for the N state. This is exactly the estimate of the cross-flow force coefficient due to the bistability for Ahmed bodies of different aspect ratios[40], it is also the same values as those reported for the side force exerted on the Windsor body during the bi-stable dynamics[29].

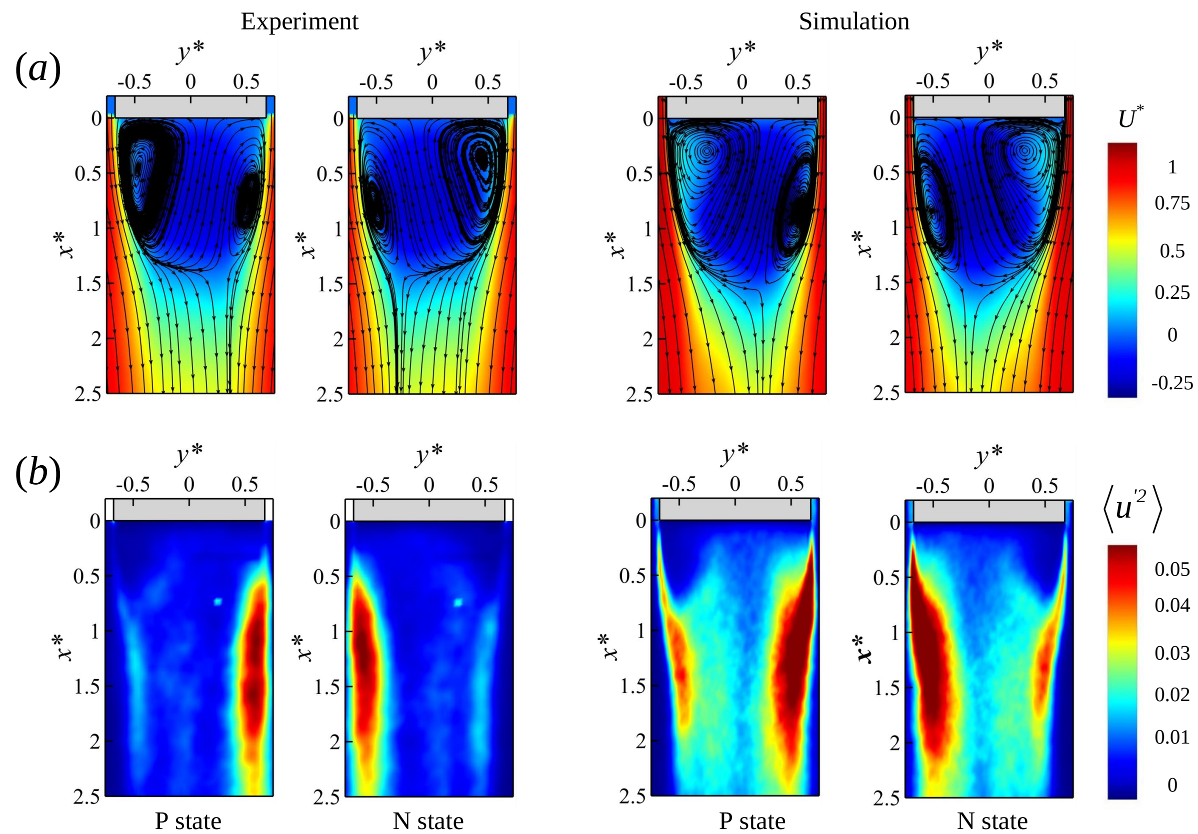


FIG. 8. Conditional averaging (see text) velocity field (a) and Reynolds stress component (b) for the experiment and the simulation. For each pair of mirrored states, left is P state and right, the N state.

## B. Conditional averaging and mean flow

The P and N states of the wake are extracted using conditionally averaged velocity field and Reynolds stress component in the $z^* = 0.67$ plane, they are shown in Fig. 8 for the experiment and the numerical simulation. The conditional averaging method is based on the barycentre of momentum deficit shown in Fig. 5, where the P (resp. N) state is the average of all PIV snapshots such that $y_w^* > 0$ (resp. $y_w^* < 0$). The thicker boundary layers observed in Fig. 8(a) at the trailing edge of the experimental case compared to the simulation might be due to the PIV resolution, since the interrogation window size is about 0.05 in non-dimensional units, it is then no possible to conclude on the shear thicknesses comparisons. At first glance the mean wake states topology in Fig. 8 are globally similar between the experiment and the simulation and in general good agreement to all published results[6,11,21] who characterized the P and N state of this flow. Some significant differences can be seen in the bubble recirculation length and Reynolds stress intensity. The longer

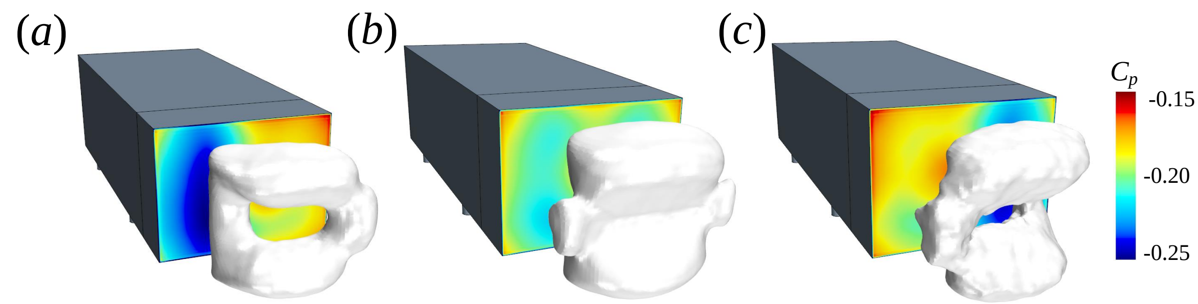


FIG. 9. Conditional averaging (see text) of the base pressure distribution and Iso-surface of pressure coefficient $Cp = -0.28$ from simulation: (a) P state; (b) Switching configuration; (c) N state.

recirculation bubble observed for the CFD is associated with lower mean flow curvature than the experiment. Actually, for inviscid steady flows, lower curvature creates lower base suction[41]. The higher base suction of $C_b = 0.203$ in the simulation against $C_b = 0.185$ in the experiment reveals the contribution of the fluctuations shown in Fig. 8(b) to the base suction, that are more intense in the simulation than in the experiment. These differences in the wake properties could be related to the absence of fore-body separation in the simulation.

Conditional averaging is now applied to the instantaneous pressure data of the computation in order to achieve a three-dimensional characterization of the wake states. In this case, the sorting criterion is based on the sign of side force coefficient filtered at 5 Hz shown in Fig. 7. A state P corresponds to the mean wake such that $C_s < -0.01$, a state N such that $C_s > 0.01$ and the switching configuration such that $|C_s| < 0.01$. Fig. 9 shows the isosurface $C_p = -0.28$ of the conditioned mean pressure field and evidences the tilted low pressure torus[8,21] of the P and N states as well as a symmetric flow from wake switching only. The left or right side of the low pressure imprint on the base corresponds to the torus approaching the model base[8,21].

We now turn to mean flows computed from a duration such that the P and N states are equiprobable. In this case, mean flows are expected to respect the reflectional symmetry $y^* \to -y^*$ as can be stated in Fig. 10 for the streamwise component of the velocity and in Fig. 11 for mean base pressure distribution. As discussed above, the simulation leads to a longer recirculation bubble (values are reported in Table II). The mean pressure distribution at the base, regardless of experiment or simulation results, as shown in Fig. 11, reveals the presence of a comparatively high-pressure region approximately at the center of the base, surrounded by a lower pressure area. This distribution results from the pressure imprint of the circular vortex ring first evidenced by

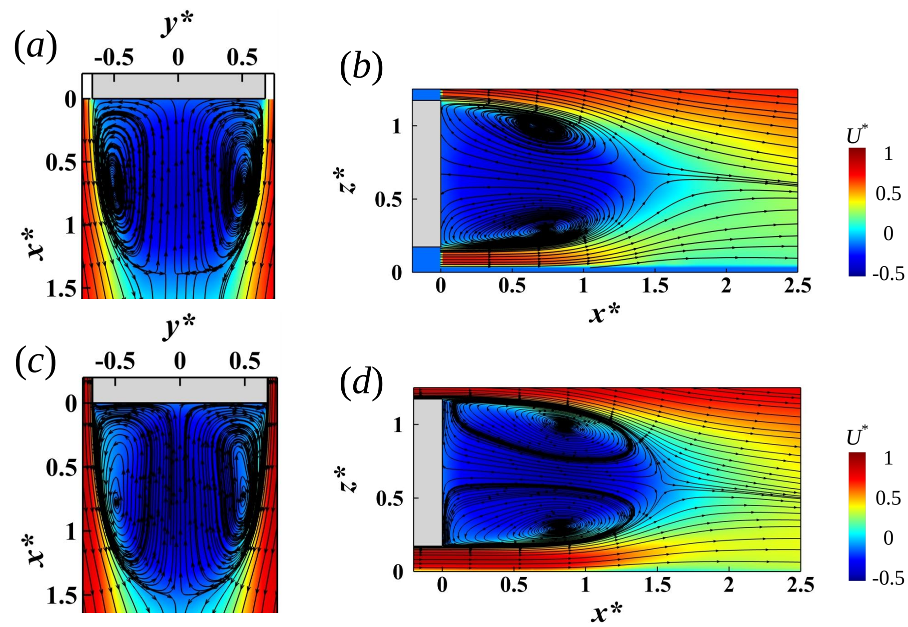


FIG. 10. Time-averaged of the streamwise component of flow field in the $z^* = 0.67$ plane (a,c) and $y^* = 0$ plane (b,d) from experiment (a,b) and simulation (c,d).

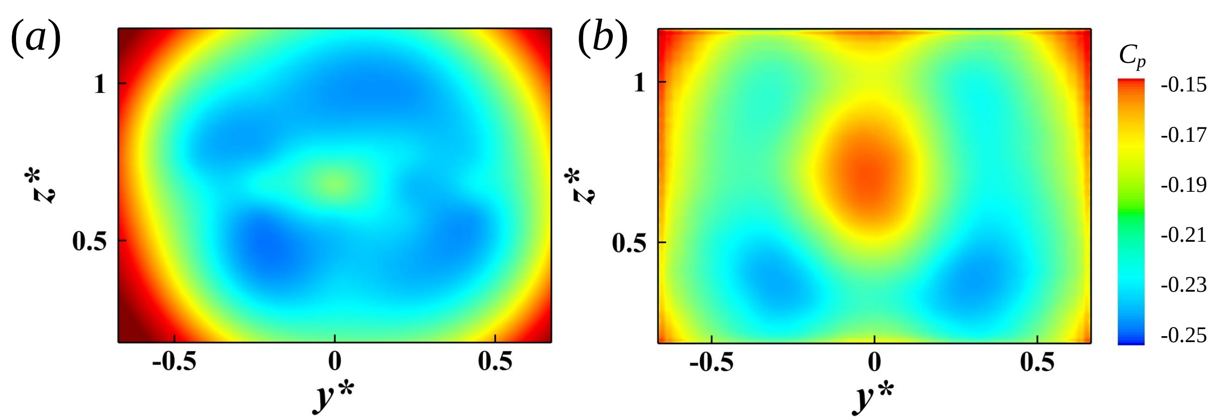


FIG. 11. Time-averaged base pressure distribution: (a) experiment; (b) simulation.

Roumeas *et al.*[42]. The pressure distribution of the simulation is much more detailed than that of the experimental one, with a clear asymmetry in the vertical direction. On the other hand, the experimental distribution seems axisymetric about the centre of the base. While the experimental distribution results from about over 60 switching between states, the simulation only have 1 and there is clearly a lack of statistical convergence in that case. A plausible explanation for the pressure distribution discrepancy is the wide variety of switching events[40], related to the diffusive phase dynamics[16,43] of the wake including random phase jumps and stochastic rotations. In addition, the poor reflectional symmetry of the experimental pressure distribution in Fig. 11(a), indicates a large sensitivity of the mean base pressure distribution to residual symmetry defects.

### C. Global dynamics

The typical global unsteady flow phenomena occurring in the wake reported in the literature[6,11,23,44] including the periodic modes in both vertical and horizontal directions, the pumping motion and the bi-stability, are now investigated using Proper Orthogonal Decomposition analysis performed on both the experimental and computed planar velocity fields, all displayed in Fig. 1(e). POD involves breaking the flow-field up into a number of optimal, orthogonal spatial modes, based on their kinetic energy content. Briefly, the first step is to calculate the planar mean velocity fields $\vec{U}^*(i,j)$ in the $k$-plane (shown in Fig. 10 for the $y$ and $z$-plane) with $i,j,k = x,y,z$ and $i \neq j \neq k$ which is then removed from each of instantaneous snapshots $\vec{u}^*(i,j,t^*)$. The rest of the analysis works on the fluctuating components of the velocity:

$$\vec{u}^*(i,j,t^*) = \vec{U}^*(i,j) + \sum_{n=1} a_n(t^*)\vec{U}_n^*(i,j), \quad (9)$$

where $a_n$ is the temporal coefficient of the $n^{\text{th}}$ POD mode $\vec{U}_n^*$. The spatial modes $\vec{U}_n^*$ are orthogonal (and can be made orthonormal), i.e. for each component of the mode, $U_{n\ell}^*$ with $\ell = x,y,z$, we have

$$\int U_{n\ell}^*(i,j) \cdot U_{m\ell}^*(i,j)didj = \delta_{nm}. \quad (10)$$

We recall that the sampling rate in experiment and simulation was 1.25 Hz and 250Hz respectively. A total of 1000 PIV snapshots (800 s physical time) with only two components of the velocity fields were sampled for the POD analysis in each plane section, which was considered to be adequate for the present analysis. Whereas for IDDES, the three components of the velocity fields from $t^* = 1528$ to $t^* = 4306$ (displayed by vertical dashed line in Fig. 6(b)) was selected for POD analysis (2500 snapshots for one plane), which ensures the symmetry of the processed data. Fig. 12 shows the turbulent kinetic energy $k_n = 1/3(U_n^2 + V_n^2 + W_n^2)$ contribution of the first fifty POD modes in the different planes displayed in Fig. 1(e). The energy proportion of each mode is higher in the experiment than in the numerical simulation because the cross-plane velocity component is missing in the PIV measurements[44]. Regardless of experiment or numerical simulation,

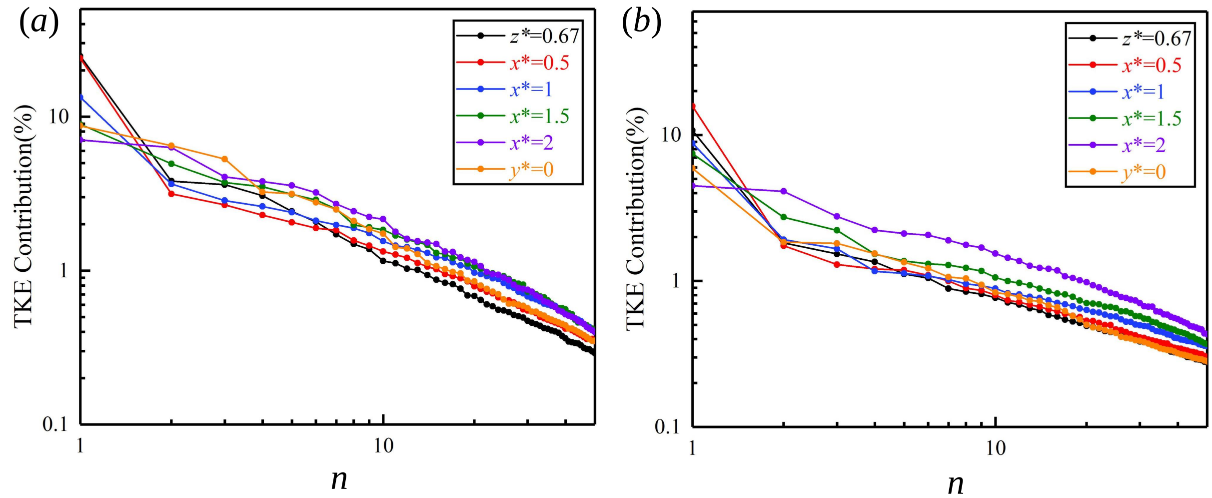


FIG. 12. Turbulent kinetic energy (TKE) contribution of POD modes 1–50 at different planes of velocity: (a) Experiment; (b) Simulation

the first-order modal energy accounts for a considerable proportion for the $x^* = 0.5$ plane (24% for the experiment, 15.7% for the simulation) and $z^* = 0.67$ plane (24.7% for the experiment, 10.8% for the simulation).

The wake dynamics is explored by phased-averaged low-order modelling of the wake flow, which has been successfully performed in our previous study[34,45–47] on the wake dynamics of kinds of cylinders (circular or twisted cylinders and porous cylinder) and a high-speed train. In the following, known global dynamics are first identified in the most significant spatial POD modes of the experiment and the simulation. Temporal coefficient are then analysed and the corresponding global dynamics are reconstructed by considering only the identified modes in Eq. (9). When reconstructions give very similar results for both the experiment and the simulation, they are only shown for the experiment.

### *1. RSB modes and Bi-stability*

Fig. 13(a,b) presents the first mode pattern from the velocity field in the plane at $z^* = 0.67$ represented by its $x$ component $U_1^*$. This mode is anti-symmetrical around $y^* = 0$, associated with higher momentum deficit on the side $y^* < 0$ compared to the other side as studied in Sec. III A. The first POD mode thus represents the reflectional symmetry breaking mode responsible for the

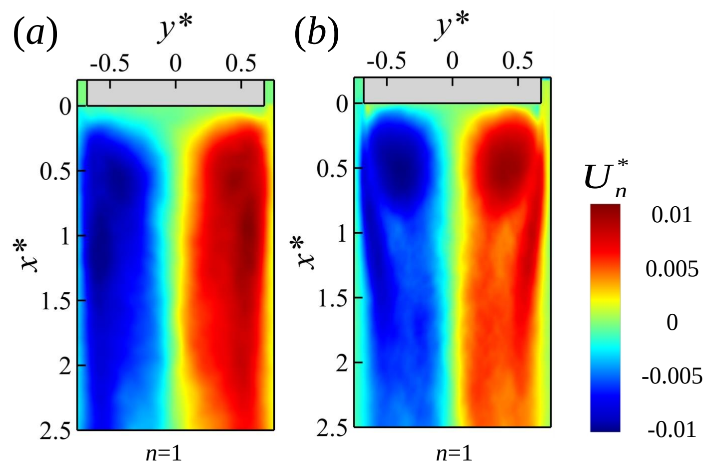


FIG. 13. Component in $x$ of the first POD mode $U_1^*$ of the (a) experimental and (b) simulated velocity field in the $z^* = 0.67$ plane.

bi-stable dynamics in both the experiment and the simulation.

The flow dynamics produced by the first POD mode can be visualized by reconstructing the flow field (low-order modelling) considering Eq. (9) with $n = 1$ only. These global dynamics consist in switching between the P and the N state of the wake. Three stages of the dynamics can be reproduced by a conditional averaging of the temporal coefficient shown in Fig. 14(a,b). The P state is retrieved considering the averaged coefficient $\langle a_1 \rangle_P$ such that $a_1 < -0.5$ in Fig. 14(c) and the N state $\langle a_1 \rangle_N$ such that $a_1 > 0.5$ in Fig. 14(e). The symmetric flow that is explored during switching or switching attempts is computed in Fig. 14(d) considering the average $\langle a_1 \rangle_S$ such that $|a_1| < 0.5$. Fig. 15(a) shows the auto-power spectra at two hot-wire points in the experimental wake, the spectrum decreases for very low frequencies with an approximately -2 power law as the consequence of the switchings, which is compatible with the previous research[6,11]. This can also be observed in the auto-power spectra of the first mode coefficient from numerical simulation, as show in the Fig. 15(b). The presence of the low frequencies as an approximately -2 power law, is the consequence of the Fourier transform of the step signal in Fig. 13(b).

### 2. *Periodic modes*

The weak coherent quasi-periodic oscillations in the vertical and lateral directions are now investigated. Fig. 16 shows the $x$ component of the second $U_2^*$ and fourth $U_4^*$ POD mode of the

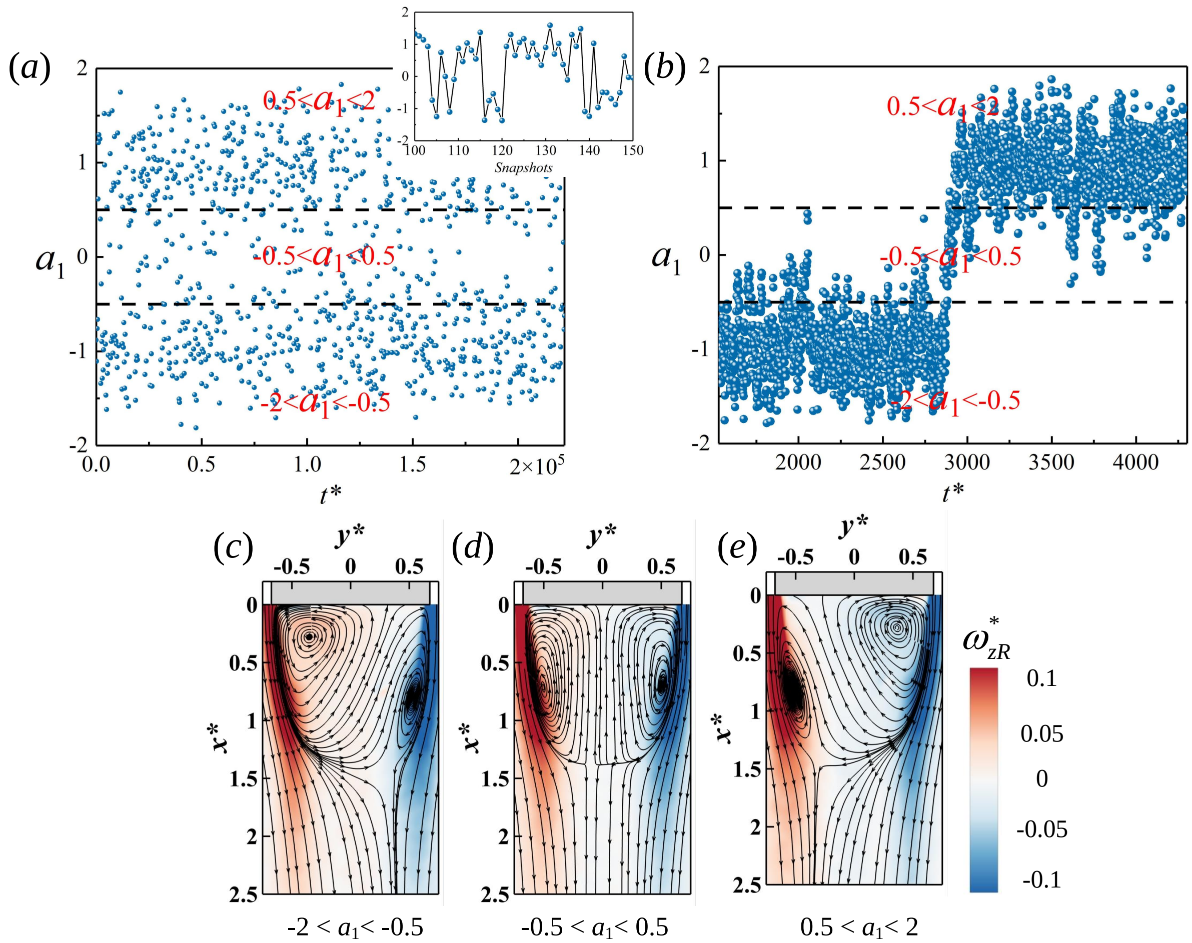


FIG. 14. Phase partition for the POD coefficient of the first mode for experiment (a) and simulation (b) at $z^* = 0.67$; (c) P state, $\vec{u}_R^{*P} = \vec{U}^* + \langle a_1 \rangle_P \vec{U}_1^*$; (d) Switching state $\vec{u}_R^{*S} = \vec{U}^* + \langle a_1 \rangle_S \vec{U}_1^*$; (e) N state $\vec{u}_R^{*N} = \vec{U}^* + \langle a_1 \rangle_N \vec{U}_1^*$. In (c,d,e) the reconstructed flow $\vec{u}_R^*$ is made for the experiment and represented by its streamlines superimposed to its vorticity $\omega^*_{zR}$.

experimental velocity field (Fig. 16a) and the POD modes $U_2^*$ and $U_3^*$ of the numerical simulation (Fig. 16b) in the horizontal direction (i. e. $z^* = 0.67$ plane). For the experiment, the flow patterns of $U_2^*$ and $U_4^*$ are quite similar with an anti-symmetry about $y^* = 0$, except for a $\pi/2$ phase shift. For the numerical simulation, $U_2^*$ and $U_3^*$ are respectively consistent with $U_2^*$ and $U_4^*$ in the experiment. Similarly, a pair of modes with the above characteristics can also be detected in the vertical direction (i. e. in the $y^* = 0$ plane), and the results from experiment and simulation are again in good agreement, as show in Fig. 17.

In the following, the dynamics of the second and fourth modes from experiment will be ex-

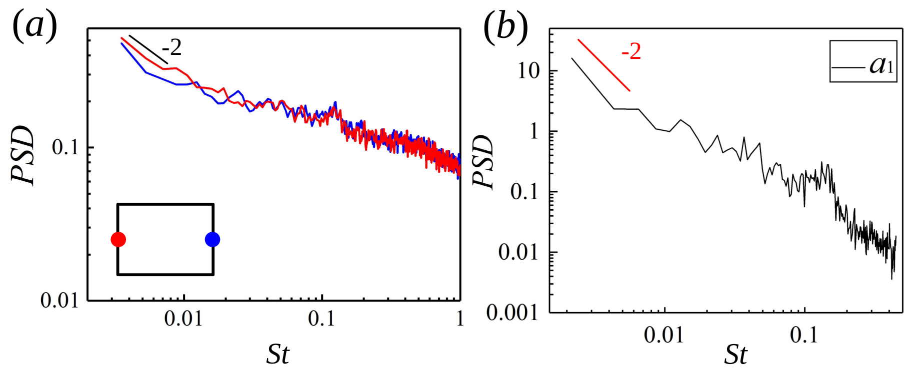


FIG. 15. Frequency characteristics of the bi-stability: Auto-power spectra at two hot-wire points at $x^* = 0.5$ in the wake (a) and the first mode coefficient from simulation (b).

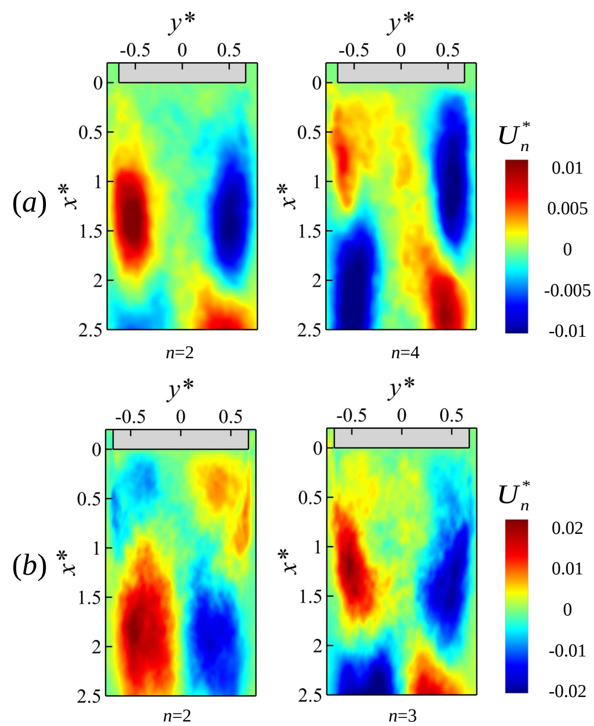


FIG. 16. Component in $x$ of the pair of quasi-antisymmetric POD modes of the (a) experimental and (b) simulated velocity field in the $z^* = 0.67$ plane having a $\pi/2$ phase shift in the streamwise direction.

plored by phase-averaged reconstruction flow field in the horizontal direction. Fig. 18(a) shows the scatter plots of the normalized temporal coefficients ($a_2$ and $a_4$) related to the second and fourth mode shown in Fig. 16(a). The temporal POD coefficients could be reordered in phase defined as $\theta = \arctan(a_4/a_2)$ as shown in Fig. 18(b) and then averaged[28,47–49] in bins of $1/4\pi$ to

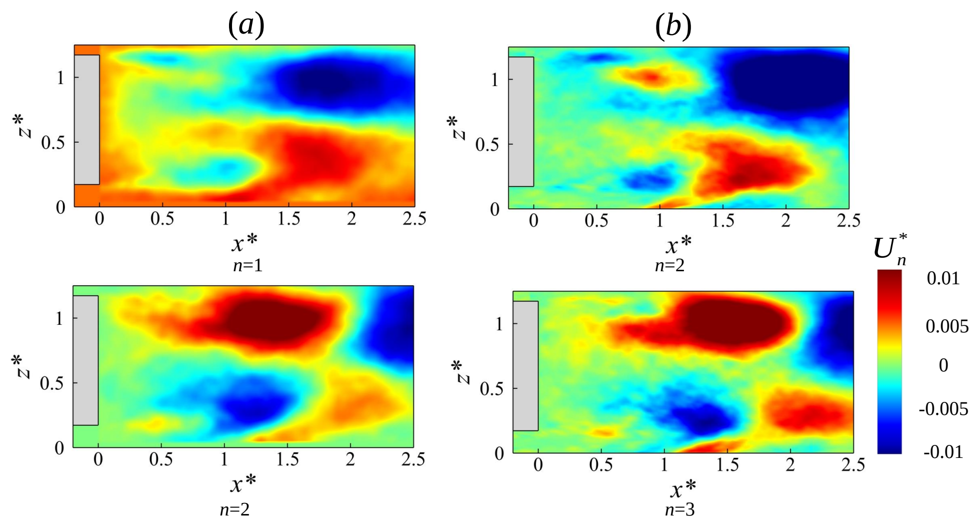


FIG. 17. Component in $x$ of the pair of quasi-antisymmetric POD modes of the (a) experimental and (b) simulated velocity field in the $y^* = 0$ plane having a $\pi/2$ phase shift in the streamwise direction.

provide $< a_2 >_\theta (\theta)$ and $< a_4 >_\theta (\theta)$ used for the reconstruction. The reconstructed flow field is shown in Fig. 19. The wake oscillation in the horizontal plane can be obviously noted from the displacement of the free stagnation point (red cross symbol) at different phases resulting in an asymmetrical wake. However, the distance to the base only exhibits slight difference for the left and right vortex core, suggesting a weaker dynamic effect on the base pressure compared to the bi-stable behavior (see Fig. 14). Using the same procedure of reconstruction, wake oscillations can also be retrieved in the vertical direction, but not shown here for conciseness.

Figs. 20(a,b) present the spectra of the global oscillation mode coefficients (second and third mode) from numerical simulation. A peak at $St = 0.145$ and $St = 0.194$ can be noted, respectively. The hot wire experiment also detects the relevant characteristic frequencies $St = 0.125$ and 0.174, as shown in Figs. 20(c,d), for four hot-wire points. In both the numerical and experimental cases, the larger oscillation frequency is observed in the vertical direction as expected by the small separating distance $H$ between interacting shears, while the smaller frequency is observed in the horizontal direction as expected by the large separating distance $W$. The obtained values are very consistent with previous measurements of Grandemange *et al.*[6] who obtained 0.127 and 0.174 for same geometry and Reynolds number. However the periodic modes frequencies are slightly larger for the simulation than for the experiments. It could be a direct consequence of the different fore-body flows, which implies different natures of the boundary layers before separation known

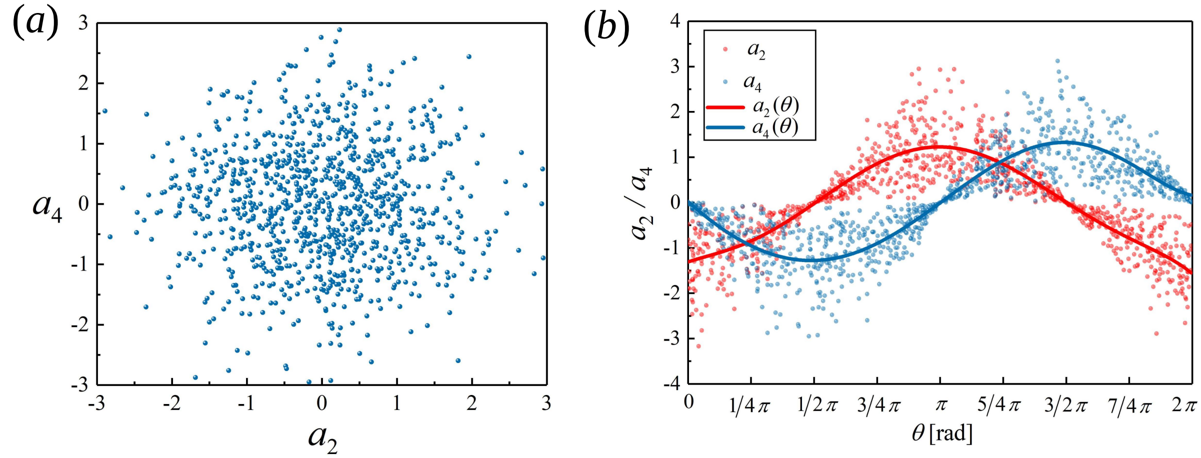


FIG. 18. The temporal coefficients of second and fourth mode in the $z^* = 0.67$ plane from experiment: (a) scatter plot of $a_4(t^*)$ vs. $a_2(t^*)$; (b) values of $a_4$ and $a_2$ sorted along the phase angle $\theta = \arctan(a_4/a_2)$ and the phase-averaged temporal coefficients $\langle a_2 \rangle_\theta$ and $\langle a_4 \rangle_\theta$.

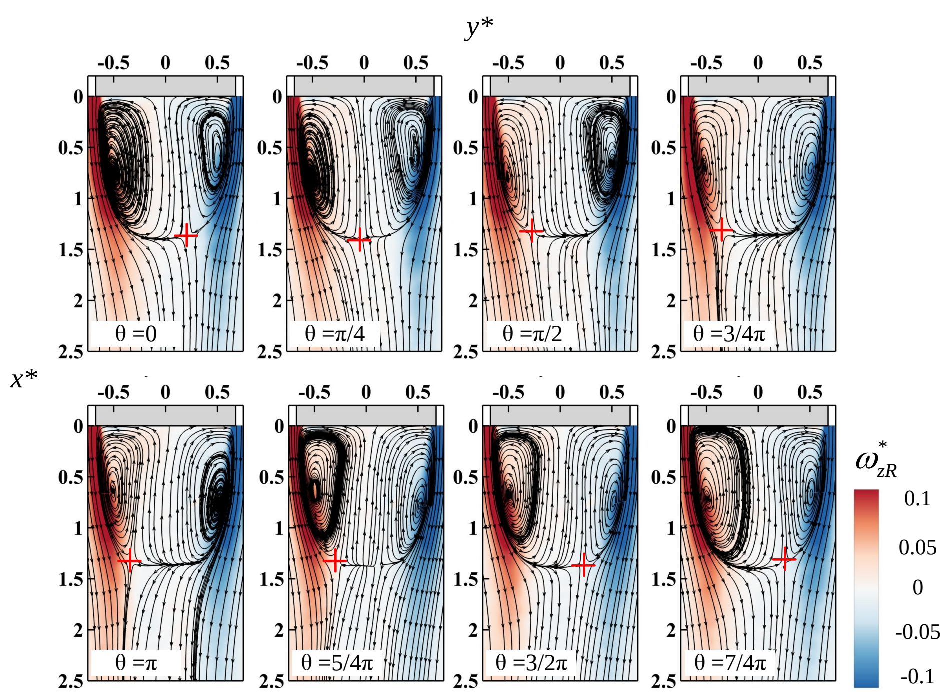


FIG. 19. Global oscillation in the $z^* = 0.67$ plane reconstructed by the second and fourth mode of the experimental velocity field, $\vec{u}^*_R = \vec{U}^* + \langle a_2 \rangle_\theta \vec{U}^*_2 + \langle a_4 \rangle_\theta \vec{U}^*_4$. The reconstructed flow $\vec{u}^*_R$ is represented by its streamlines superimposed to its vorticity $\omega^*_{zR}$.

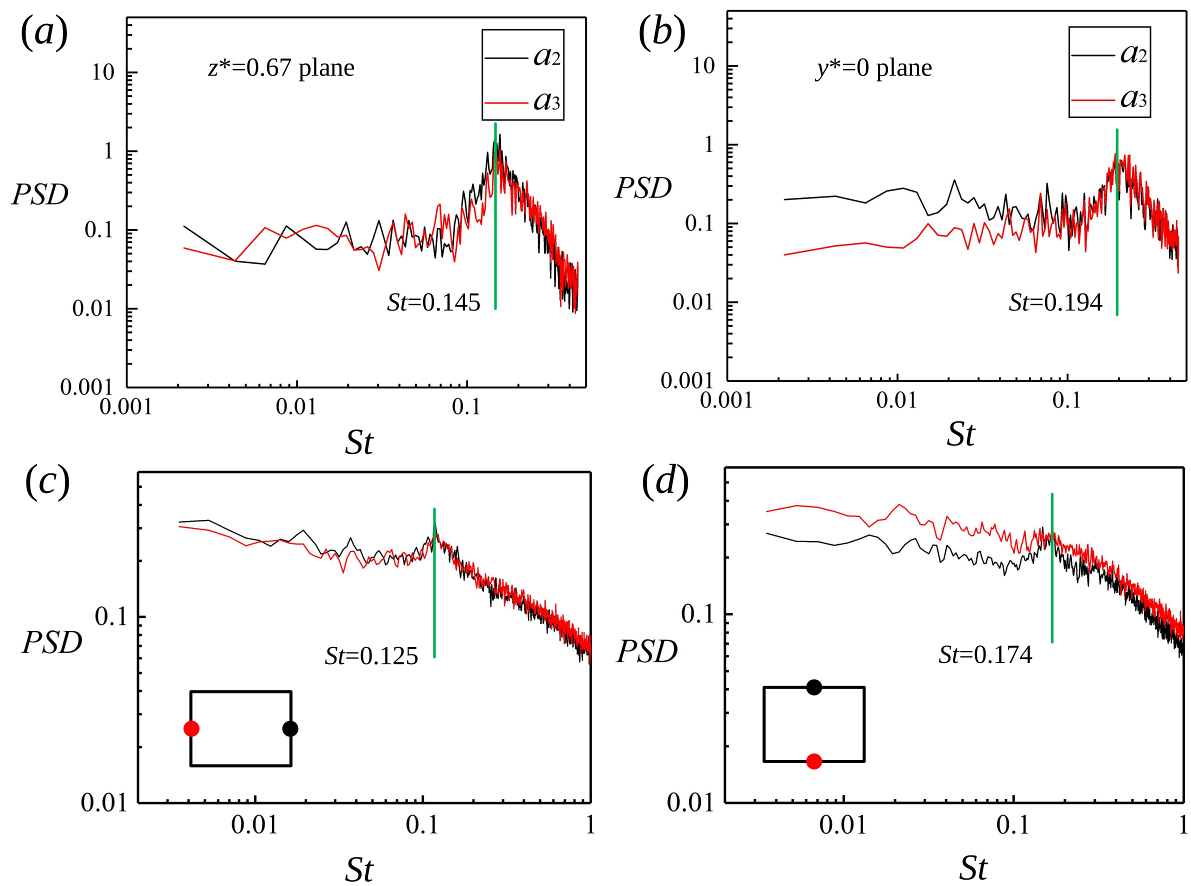


FIG. 20. Auto-power spectra of hot-wire points at $x^* = 2$ in the wake for experiment results: (a) horizontal direction; (b) vertical direction; and the second and third mode coefficient from simulation: (c) $z^* = 0.67$; (d) $y^* = 0$.

to affect the Strouhal number[50].

### 3. *Pumping motion*

As shown in Fig. 21(a), the third mode extracted from the experimental data in the horizontal plane presents the characteristic of left and right symmetry, exhibiting different sign of the pulsation velocity between the middle and two sides in the wake. According to the experimental result, the fourth mode extracted from the simulation data has a similar feature, as shown in Fig. 21(b). In the vertical plane, the experimental third mode and the simulated fourth mode present a top and bottom symmetry, as shown in Fig. 21(c,d). Due to their symmetry properties, these POD modes are able to produce a dynamics of elongation and shortening of the recirculating bubble in

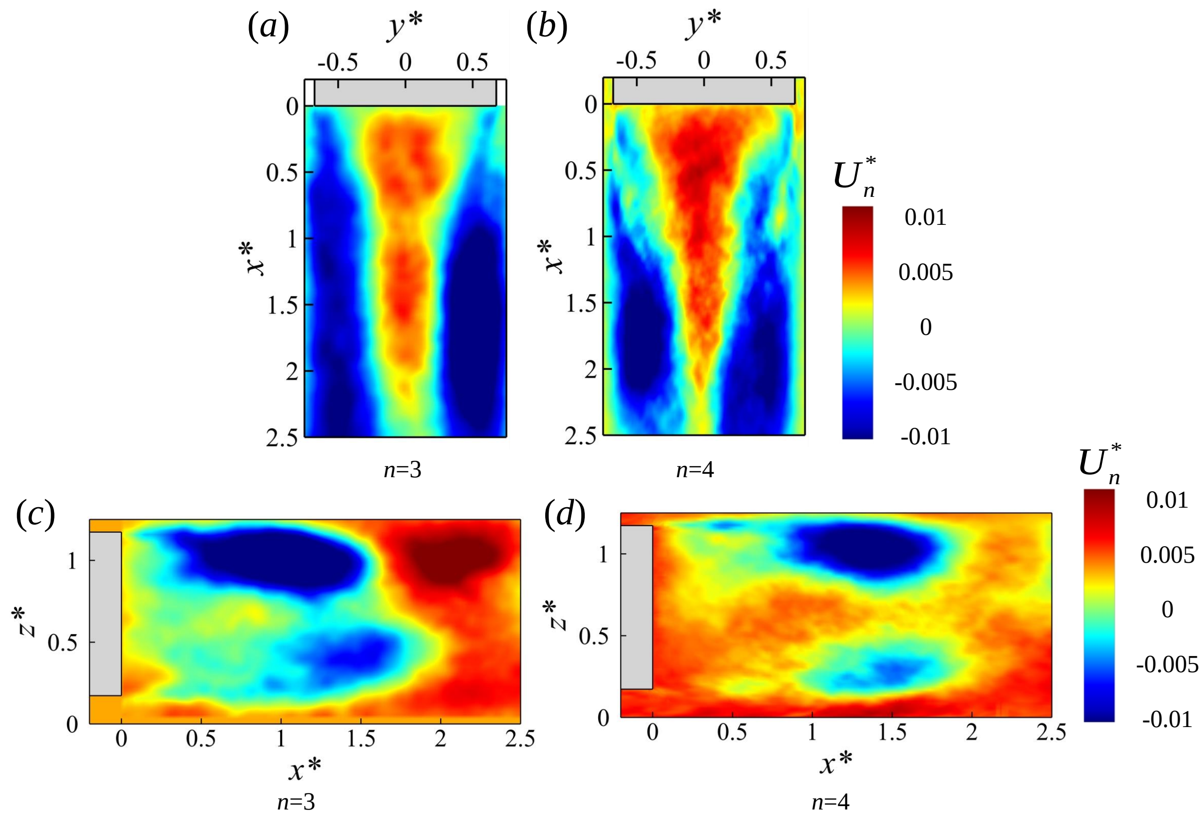


FIG. 21. Component in $x$ of the quasi-symmetric POD mode $U_3^*$ of the (a,c) experimental and $U_4^*$ of (b,d) simulated velocity field in the (a,b) $z^* = 0.67$ and (c,d) $y^* = 0$ planes.

the streamwise direction, refered to as the pumping motion in the literature. Fig. 22 shows the experimental and the simulated conditional-averaged velocity field reconstructed by the third mode at $y^* = 0$ with $a_3$ averaged in the bins defined in Fig. 22(a,b). As revealed in Figs. 22(c,d), the position of the free stagnation point shifts from $x^* = 1.3$ to $x^* = 1.5$ in the streamwise direction, leading to the pumping behavior. A striking observation in Fig. 22(c,d) is that, at the maximum length of the bubble, a vortex structure appears at the upper shear layer for both the experiment and the simulation. It is noteworthy that no such vortex structure is detectable in the horizontal plane reconstruction while the pumping motion is clearly observable (not shown in the paper for succinctness).

Although the pumping behavior has been confirmed in the reconstruction flow in Fig. 22, no peak frequency at $St = 0.08$ as reported by Volpe *et al.*[11] can be detected in the spectra of the corresponding POD mode from the simulation, as shown in Fig. 23 (a,b). In terms of the spectra of 116 hot wire velocity signals in the wake, no obvious peak frequency has been detected in the

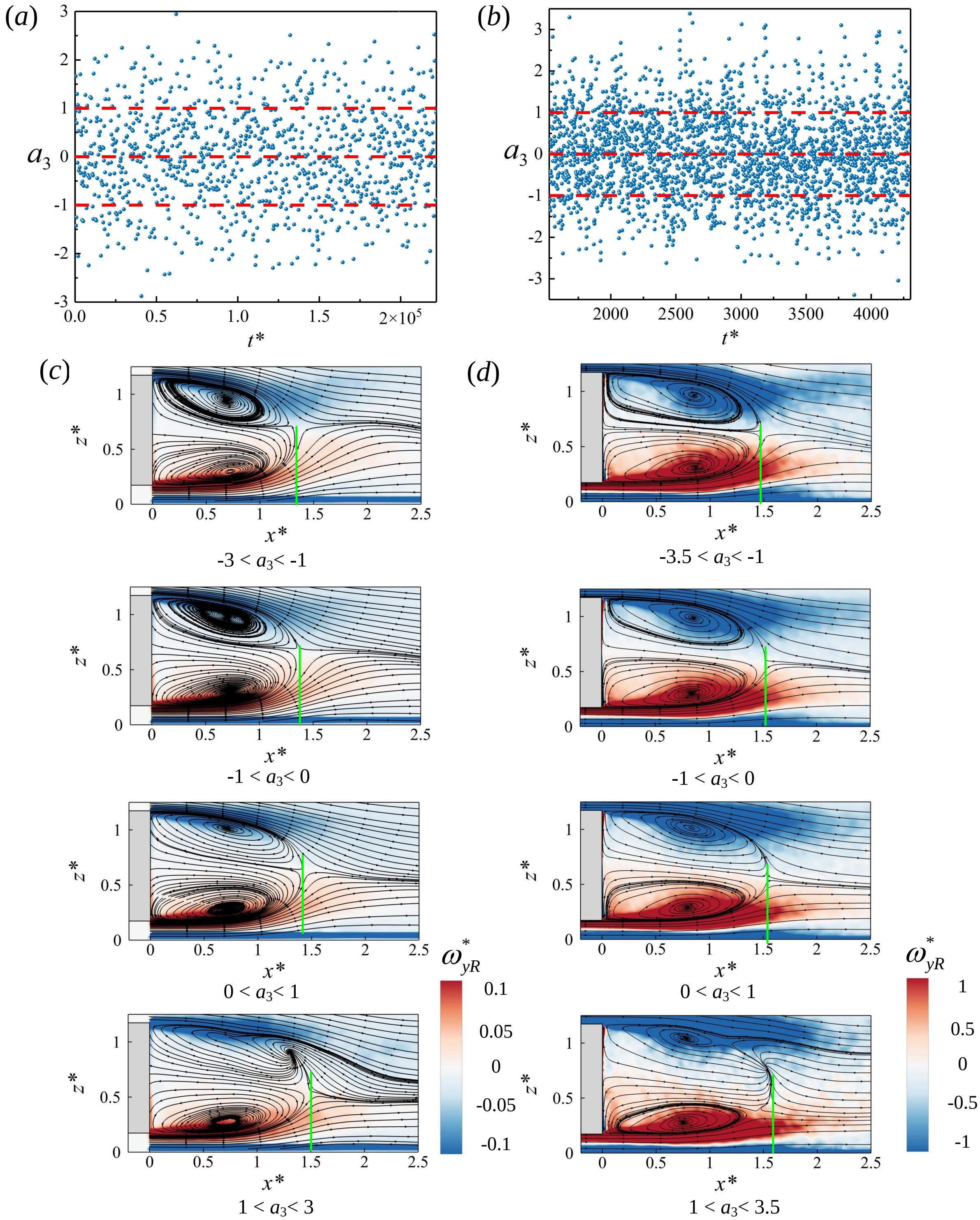


FIG. 22. Pumping motion in the $y^* = 0$ plane reconstructed by the third mode from conditional averaging of the temporal coefficient of (a) experimental and (b) simulated velocity field. The reconstructed flow $\vec{u}^*_R = \vec{U}^* + \langle a_3 \rangle_{a3} \vec{U}^*_3$ is represented by its streamlines superimposed to its vorticity $\omega^*_{yR}$ in (c) for the experiment and (d) for the simulation.

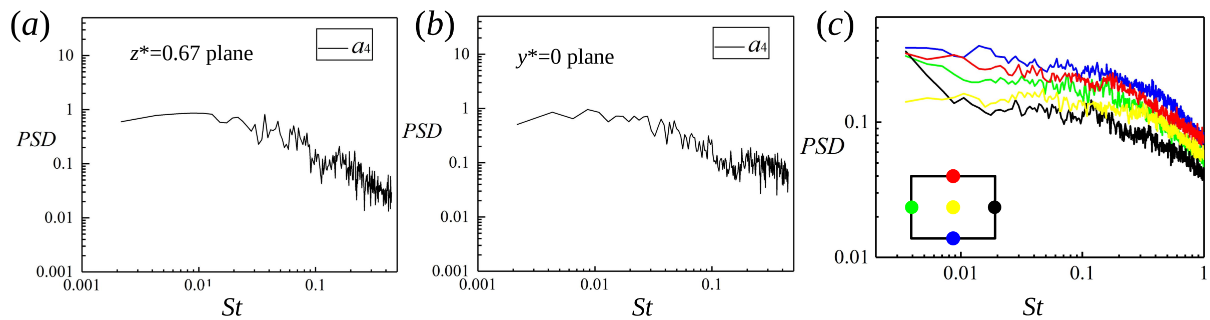


FIG. 23. Auto-power spectra of the temporal coefficient $a_4$ associated with the pumping motion at (a) $z^* = 0.67$ and at (b) $y^* = 0.$ ; and (c) five hot wire points in the wake at $x^* = 1.5$.

low frequency band as can be seen in Fig. 23(c) for five hot wire points (the rest of the results are not shown here). It is plausible that the pumping behavior in the recirculation region is not a quasi-periodic phenomenon but affect the whole spectrum at low frequencies, which should be confirmed further.

## IV. WAKE SWITCHING

In this section, the interactions among the flow modes stated above will be investigated. POD analysis and low-order modes reconstruction of cross-flow planes are conducted again on both the experimental and simulation data. In order to have an insight into the bi-stable switching process of both approaches we follow the same analysis of fields reconstruction as in Pavia *et. al*[28]. In addition, 3D instantaneous snapshots obtained in the numerical simulation during the bi-stable transition are shown for completeness.

The 4 cross-flow planes shown in Fig. 1(e) have been analysed. From the TKE contributions in Fig. 12, it can be seen for the experiment and the simulation that the first-order modal energy reduces gradually when moving downstream, implying that the bi-stable phenomenon characterized by the first mode $n = 1$ mainly acts in the near wake region, before the recirculation closure. On the contrary, the higher order modes energy for $n \geq 2$ increases when moving downstream indicating that periodic modes and pumping motion mainly acts after the recirculation closure. Only results in the plane $x^* = 1.5$ is presented as no more relevant information was obtained in the other planes.

Fig. 24(a,b) shows the patterns of the first three POD modes extracted from experiment and

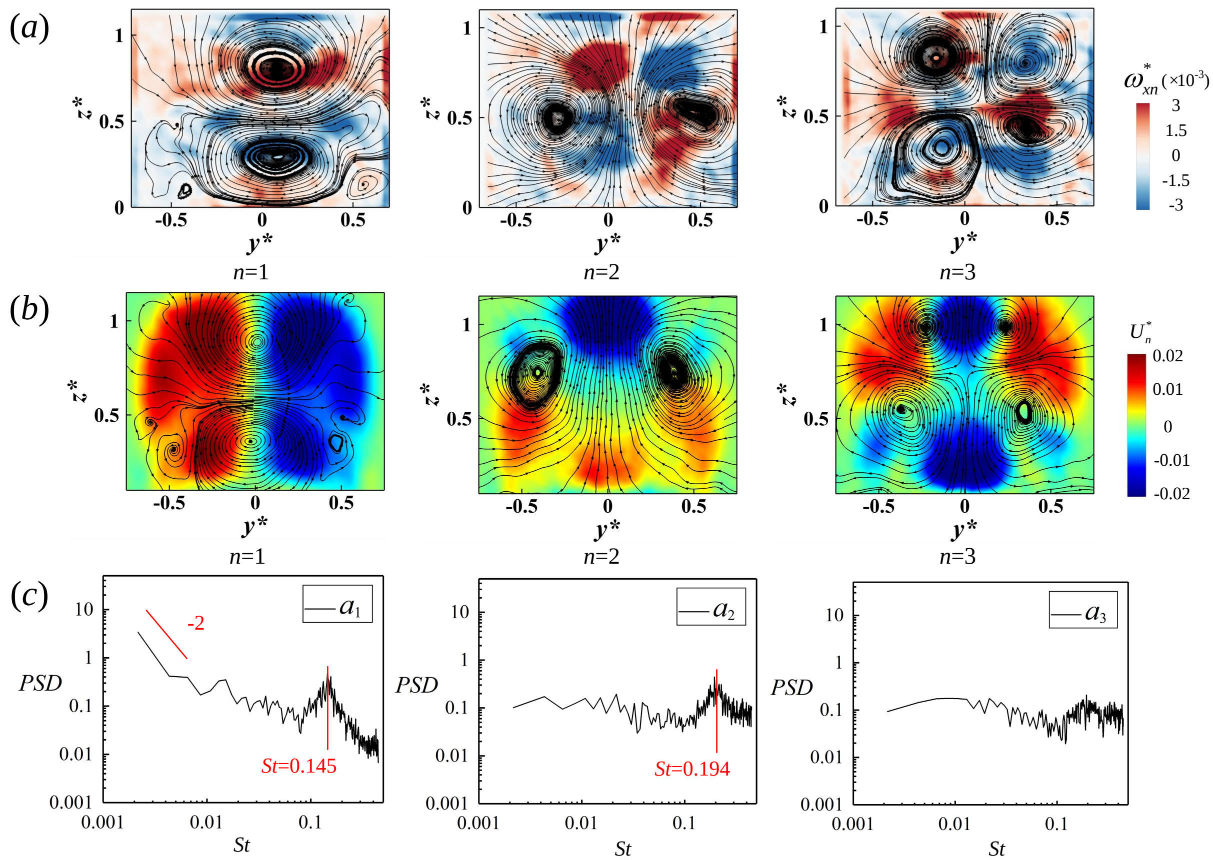


FIG. 24. The first three POD modes $\vec{U}_1^*$, $\vec{U}_2^*$ and $\vec{U}_3^*$ for the (a) experimental and (b) simulated velocity field in the $x^* = 1.5$ plane. Auto-power spectra (c) of the corresponding temporal coefficients obtained in the simulation.

simulation. The modes contour is represented by the $x$-component of the velocity in the numerical simulation, and by the streamwise vorticity component in the experiment (because the $x$-component of the velocity is not measured with the planar PIV). There is a very good correspondence between experiment and simulation in the modes topology as can be seen by comparing the streamlines. They are also in accordance with the POD modes found in Pavia *et. al*[28]. The associated global dynamics can be easily identified in the power spectral density of their temporal coefficients in Fig. 24(c) that can only be obtained for the simulation having the required time resolution. Hence, the first mode captures both the RSB mode (switching dynamics with a -2 power law) and the periodic mode in the horizontal direction (resonant peak at $St = 0.145$), while the second and third modes capture essentially the periodic mode in the vertical direction (resonant peak at $St = 0.194$).

We now follow the same reconstruction procedure as Pavia *et. al*[28] based on the phase $\theta = \arctan(a_2/a_1)$ by making a phase averaging of the temporal coefficients $a_1$, $a_2$ and $a_3$ in bins of $\theta = \pi/4$. The 3 phase-averaged coefficients are denoted $\langle a_1\rangle_\theta$, $\langle a_2\rangle_\theta$ and $\langle a_3\rangle_\theta$. The experimental reconstructed flow $\vec{u}^*_R = \vec{U}^* + \langle a_1\rangle_\theta \vec{U}^*_1 + \langle a_3\rangle_\theta \vec{U}^*_3 + \langle a_2\rangle_\theta \vec{U}^*_2$ in Figs. 25 is in agreement with results of Pavia *et. al*[28] and describes a virtual switching when the phase progresses from $\theta = 0$ (N state) to $\theta = \pi$ (P state). The cross flow measurements of Grandemange *et al.*[6] of the P state obtained from an averaging conditioned by the wake deficit barycentre is also very similar to the reconstructed flow at $\theta = \pi$. The mushroom like structure that can be identified in the N and P states corresponds to two counter rotating streamwise vortices that are now well established in the literature[51–53]. The reconstructed fields between the $\theta = 0$ and $\pi$ states take into account for real switchings but also for all switching attempts. For the experimental results, the mirror symmetry between the $\theta$ and $\theta + \pi$ fields indicates an identical general scenario whether the wake deviation occurs with $a_2 > 0$ ($0 < \theta < \pi$) or $a_2 < 0$ ($\pi < \theta < 2\pi$). This is not the case for the simulation that clearly distinguishes both cases. It is believed to be related to the small duration of the simulation compared to the experiment that might not explore the complete phase portrait of the dynamics.

The system is in an unstable equilibrium condition when it reaches $\theta \approx \pi/2$ or $3\pi/2$ and can either attempt a switching by returning to the previous state or switch to the opposite state, depending on any random perturbation[54]. Previous studies[21,28] have shown that this random disturbance might originate from the longest edges of the rectangular base. In the following, snapshots of the high-frequency samples obtained by the numerical simulation provide more detail about this perturbation.

Fig. 26 shows nine instantaneous snapshots sampled with $\delta t^* = 0.6$ of iso-contours of pressure $C_p = -0.28$ during the wake switching ($t^* = 2886.6 - 2891.4$). In addition to the low-pressure toroidal vortex structure in the near wake, a large-scale hairpin vortex is shed from the upper shear layer, which is conjectured to be responsible for triggering bi-stable switches. This similar phenomenon has ever appeared in the numerical investigation on the wake of a simplified lorry by Dalla Longa *et al.*[21]. Recently, Pavia *et al.*[53] confirmed that a pair of vortex "tails" aligned in the horizontal direction exists in the symmetric wake configuration of a square back model using tomographic PIV, which is deemed to be corresponding to the two streamwise legs of the large-scale hairpin vortex in Fig. 26. This hairpin vortex shedding is reminiscent of the vortex shedding from the upper shear layer when the recirculation length reaches its maximum value in the reconstruction flow of the pumping motion in Fig. 22(c,d) for both the experiment and the simulation.

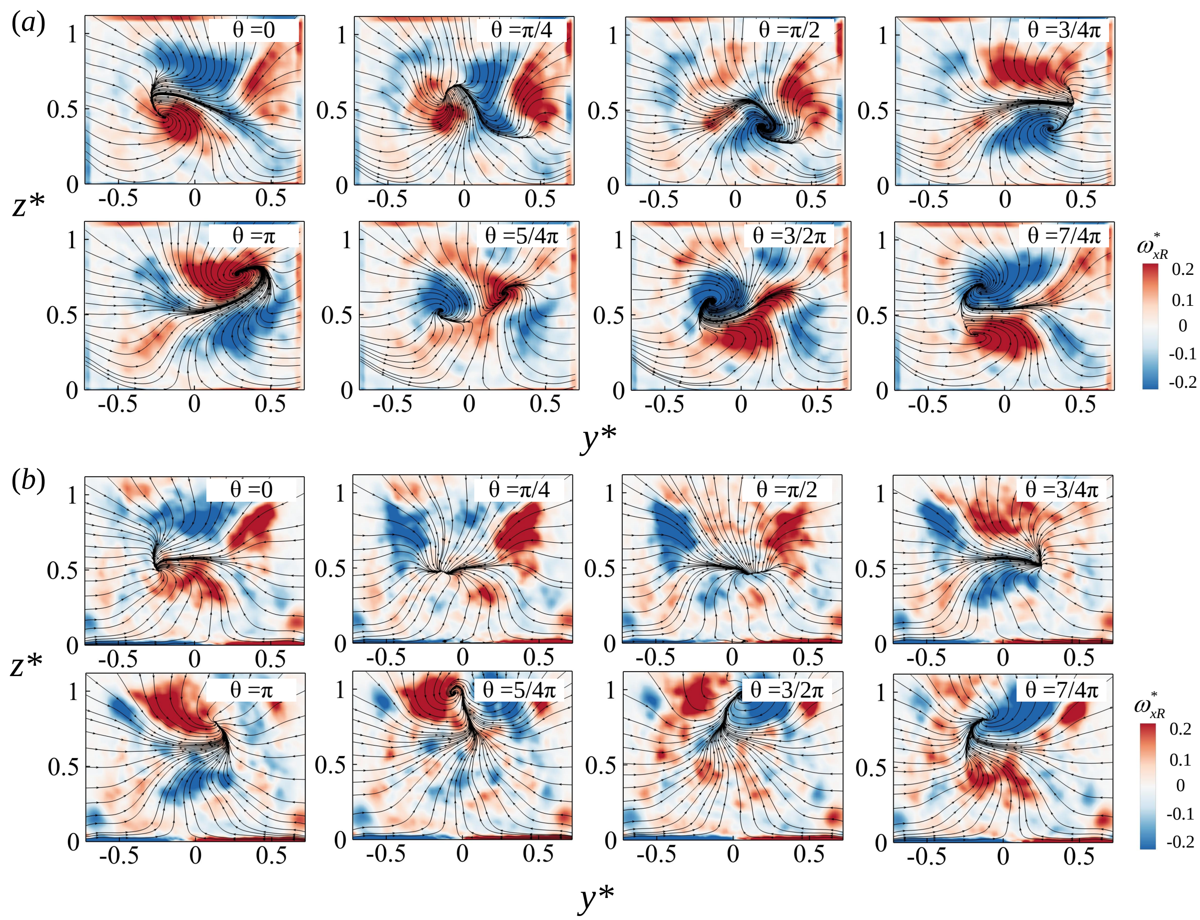


FIG. 25. Low-order phase-averaged velocity field at $x^* = 1.5$ from (a) experiment and (b) simulation. The reconstructed flow $\vec{u}_R^* = \vec{U}^* + \langle a_1 \rangle_\theta \vec{U}_1^* + \langle a_3 \rangle_\theta \vec{U}_3^* + \langle a_2 \rangle_\theta \vec{U}_2^*$ is represented by its streamlines superimposed to its vorticity $\omega_{xR}^*$

Presumably, this large-scale hairpin vortex appearing with the bi-stable switching is closely related to the pumping motion. This correlation can be found in the 3D unsteady wake structures over a wall-mounted short cylinder investigated by Zhu *et al.*[55] using tomographic PIV. They proposed that the flapping motion, i.e. oscillation of the recirculation region, has a modulating effect on the occurrence of the large-scale streamwise vortex.

Finally, a conceptual mode is proposed for the wake topology behind the square back Ahmed body, as sketched in Fig. 27, based on the analysis of numerical simulation and experimental results. The wake structure shows two types of configurations states, the asymmetric states on a long time-scale and the symmetrical state configuration on a short time scale during the switching. In both configurations, there is a vortex system composed of four vortex columns. When the wake

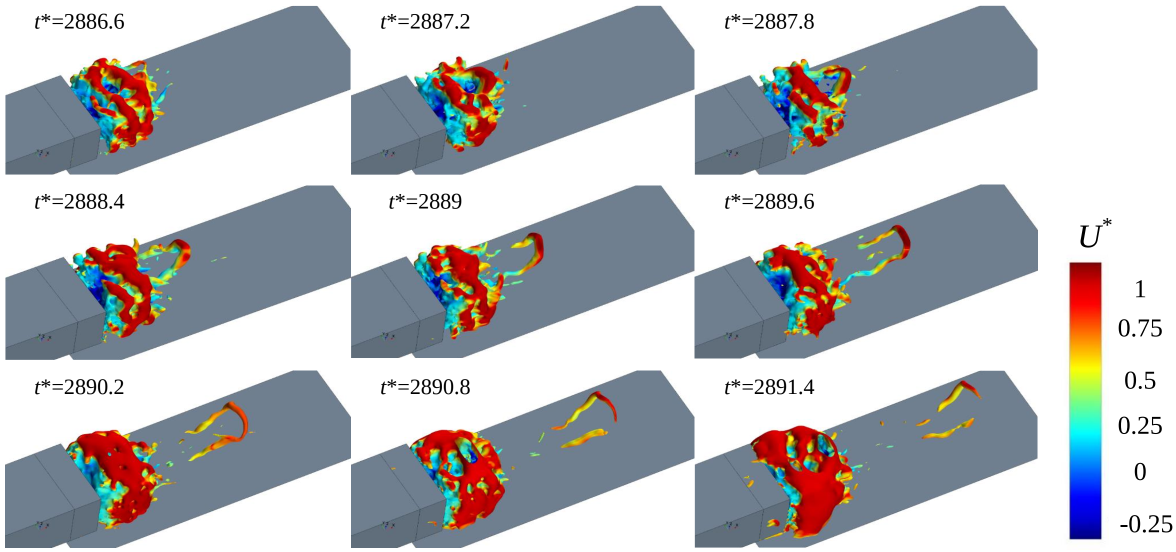


FIG. 26. Instantaneous snapshots of Iso-surface of pressure $c_p = -0.28$ coloured by the streamwise velocity.

structure is in the asymmetric states, as shown in the Fig. 27(a), the distance between the left and right vortex columns from the model base is different. There is a streamwise vortex column downstream the recirculation region, which is developed from the upstream hairpin vortex. On the other hand, the toroidal vortex structure exhibits the characteristics of global symmetry when in the symmetrical configuration, as shown in the Fig. 27(b). The most notable feature is that a hairpin streamwise vortex is generated by random arching in the upper or lower shear layer, and then falls off, when a switching between the asymmetric states occurs.

## V. CONCLUSION

An extensive experimental campaign consisting of pressure, hot-wire and PIV measurement is carried out at $Re = 9.2 \times 10^4$ to investigate the wake dynamics the square-back Ahmed body. Numerical simulation is performed by IDDES and compared to experiments and previous simulations by exploring the unstable wake. The following conclusions may be drawn: The simulation/experiment comparison shows that the numerical simulation adequately reproduces the main unsteady flow features of the wake observed in the present experimental work and that of Grandemange *et al.*[6] as well as the LES simulation of Dalla Longa *et al.*[21] despite the fact that IDDES does not capture the fore-body separations observed for this Reynolds number. It results in a more

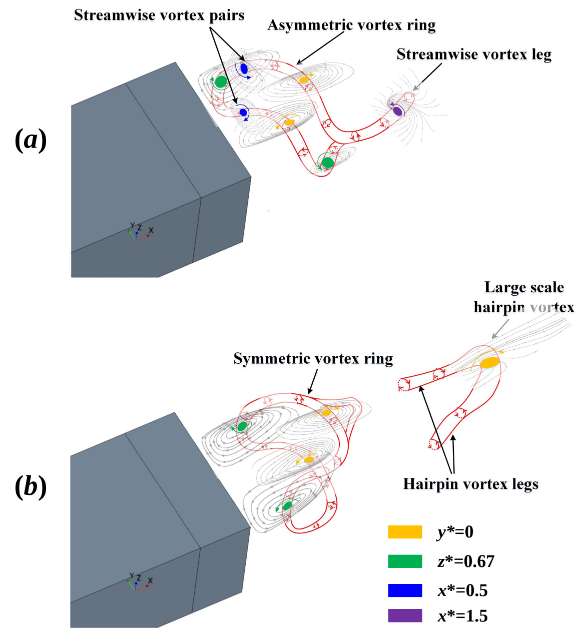


FIG. 27. Sketch of 3D bi-stable wake topology: (a) Asymmetric configuration; (b) Symmetric configuration.

intense wake, with larger base suction, base pressure gradients and fore-body friction drag as well as higher frequencies of the periodic global modes. These wake effects are likely related to the nature of the boundary layers prior the rectangular base separations that are drastically modified by the absence of fore-body separations. It is speculated that the large discrepancy of reported values of drag for square-back geometries in the literature may result from the flow around the fore-body that is rarely investigated in the papers. More fundamentally, the long-term bi-stability and the switching process in the unstable wake are successfully captured by IDDES simulation. The application of snapshot POD and spectral analysis distinguish the four global dynamics of the wake as already reported in the recent literature of the square-back Ahmed body[6,8,11,21,44,51,56] associated with the RSB mode, lateral and vertical periodic modes and the pumping motion. However, no resonant characteristic frequency was observed for both experiment and numerical results. Further insights into the interaction between the different wake modes have been offered through the application of low-order modelling and the instantaneous 3D flow field analysis. A large-scale hairpin vortex originating from the pumping motion sheds from the upper or lower shear layer, appears during the switching or switching attempt of the bi-stable dynamics. Ultimately, the results of the findings presented in this work help to build a 3D bi-stable wake topology of the square-back Ahmed body.

## ACKNOWLEDGMENTS

The authors would like to thank John Wrightson for the polishing of the manuscript. This work was supported by the National Natural Science Foundation of China (Grand No. 51905381), Shanghai Key Laboratory of Aerodynamics and Thermal Environment Simulation for Ground Vehicles (Grand No. 18DZ2273300) and Shanghai Automotive Wind Tunnel Technical Service Platform (Grand No. 19DZ2290400).

## DATA AVAILABILITY STATEMENT

The data that support the findings of this study are available from the corresponding author upon reasonable request.

## REFERENCES

[1] S. Ahmed, G. Ramm, and G. Faitin, "Some salient features of the time-averaged ground vehicle wake," SAE Technical Paper Series , 840300 (1984).

[2] S. Krajnović, "Large eddy simulation exploration of passive flow control around an ahmed body," Journal of Fluids Engineering, Transactions of the ASME **136** (2014).

[3] W.-H. Hucho and G. Sovran, "Aerodynamics of road vehicles," Annual Review of Fluid Mechanics **25**, 485–537 (1993).

[4] A. Spohn and P. Gilliéron, "Flow separations generated by a simplified geometry of an automotive vehicle," IUTAM symposium—unsteady separated flows , 1–6 (2002).

[5] B. F. Zhang, Y. Zhou, and S. To, "Unsteady flow structures around a high-drag ahmed body," Journal of Fluid Mechanics **777**, 291–326 (2015).

[6] M. Grandemange, M. Gohlke, and O. Cadot, "Turbulent wake past a three-dimensional blunt body. Part 1. Global modes and bi-stability." Journal of Fluid Mechanics **722**, 51–84 (2013).

[7] M. Grandemange, M. Gohlke, and O. Cadot, "Bi-stability in the turbulent wake past parallelepiped bodies with various aspect ratios and wall effects," Physics of Fluids **25**, 95–103 (2013).

[8] J.-M. Lucas, O. Cadot, V. Herbert, S. Parpais, and J. Délery, "A numerical investigation of the asymmetric wake mode of a squareback Ahmed body – effect of a base cavity." Journal of Fluid Mechanics **831**, 675 – 697 (2017).

[9]M. Grandemange, M. Gohlke, and O. Cadot, "Reflectional symmetry breaking of the separated flow over three-dimensional bluff bodies," Physical Review E **86**, 035302 (2012).

[10]O. Evstafyeva, A. S. Morgans, and L. Dalla Longa, "Simulation and feedback control of the Ahmed body flow exhibiting symmetry breaking behaviour," Journal of Fluid Mechanics **817**, R2 (2017).

[11]R. Volpe, P. Devinant, and A. Kourta, "Experimental characterization of the unsteady natural wake of the full-scale square back Ahmed body: flow bi-stability and spectral analysis," Experiments in Fluids **56**, 99 (2015).

[12]M. Grandemange, O. Cadot, A. Courbois, V. Herbert, D. Ricot, T. Ruiz, and R. Vigneron, "A study of wake effects on the drag of the Ahmed squareback model at the industrial scale," Journal of Wind Engineering and Industrial Aerodynamics **145**, 282–291 (2015).

[13]G. Yan, C. Xia, H. Zhou, H. Zhu, and Z. Yang, "Experimental investigation of the bi-stable behavior in the wake of a notchback mira model," SAE Technical Paper , 2019–01–0663 (2019).

[14]B. Herry, L. Keirsbulck, and J. Paquet, "Flow bi-stability downstream of three-dimensional double backward facing steps at zero-degree slideslip," ASME Transactions Journal of Fluids Engineering **133**, 1–4 (2011).

[15]D. Fabre, F. Auguste, and J. Magnaudet, "Bifurcations and symmetry breaking in the wake of axisymmetric bodies," Physics of Fluids **20**, 051702 (2008).

[16]G. Rigas, A. Oxlade, A. Morgans, and J. Morrison, "Low-dimensional dynamics of a turbulent axisymmetric wake," Journal of Fluid Mechanics **755**, 159 (2014).

[17]G. Bonnavion, O. Cadot, V. Herbert, S. Parpais, R. Vigneron, and J. Délery, "Asymmetry and global instability of real minivans' wake," Journal of Wind Engineering and Industrial Aerodynamics **184**, 77–89 (2019).

[18]E. Varon, Y. Eulalie, S. Edwige, P. Gilotte, and J.-L. Aider, "Chaotic dynamics of large-scale structures in a turbulent wake," Physical Review Fluids **2**, 034604 (2017).

[19]J. Zhang, G. Minelli, A. N. Rao, B. Basara, R. Bensow, and S. Krajnović, "Comparison of pans and les of the flow past a generic ship," Ocean Engineering **165**, 221 – 236 (2018).

[20]A. Rao, G. Minelli, B. Basara, and S. Krajnovìc, "On the two flow states in the wake of a hatchback Ahmed body," Journal of Wind Engineering and Industrial Aerodynamics **73**, 262 – 278 (2018).

[21]L. Dalla Longa, O. Evstafyeva, and A. Morgans, "Simulations of the bi-modal wake past three-dimensional blunt bluff bodies," Journal of Fluid Mechanics **866**, 791–809 (2019).

[22]J. Östh, B. Noack, S. Krajnović, D. Barros, and J. Borée, "On the need for a nonlinear subscale turbulence term in pod models as exemplified for a high-reynolds-number flow over an ahmed body," Journal of Fluid Mechanics **747**, 518–544 (2014).

[23]A. Lahaye, A. Leroy, and A. Kourta, "Aerodynamic characterisation of a square back bluff body flow," Int. J. of Aerodynamics **4**, 43 – 60 (2014).

[24]B. Khalighi, S. Zhang, C. Koromilas, S. Balkanyi, L. Bernal, G. Iaccarino, and P. Moin, "Experimental and computational study of unsteady wake flow behind a bluff body with a drag reduction device," SAE Technical Paper Series **2001-01-1042** (2001).

[25]B. Khalighi, K. Chen, and G. Laccarino, "Unsteady aerodynamic flow investigation around a simplified squareback road vehicle with drag reduction devices," Journal of Fluids Engineering **134** (2012).

[26]E. Duell and A. George, "Experimental study of a ground vehicle body unsteady near wake," SAE transactions **108**, 1589–1602 (1999).

[27]E. Berger, D. Scholz, and M. Schumm, "Coherent vortex structures in the wake of a sphere and a circular disk at rest and under forced vibrations," Journal of Fluids and Structures **4**, 231–257 (1990).

[28]G. Pavia, M. Passmore, and C. Sardu, "Evolution of the bi-stable wake of a square-back automotive shape," Experiments in Fluids **59**, 20 (2018).

[29]A. Perry, G. Pavia, and M. Passmore, "Influence of short rear end tapers on the wake of a simplified square-back vehicle: wake topology and rear drag," Experiments in Fluids **57**, 169 (2016).

[30]Y. Haffner, J. Borée, A. Spohn, and T. Castelain, "Mechanics of bluff body drag reduction during transient near-wake reversals," Journal of Fluid Mechanics **894**, 1–35 (2020).

[31]R. Pattenden, S. Turnock, and X. Zhang, "Measurements of the flow over a low-aspect-ratio cylinder mounted on a ground plane," Experiments in Fluids **39**, 10–21 (2005).

[32]H. J. Wang, H.F.and Cao and Y. Zhou, "POD analysis of a finite-length cylinder near wake," Experiments in Fluids **55**, 1790 (2014).

[33]C. Xia, H. Wang, X. Shan, Z. Yang, and Q. Li, "Effects of ground configurations on the slipstream and near wake of a high-speed train," Journal of Wind Engineering and Industrial Aerodynamics **168** (2017).

[34]Z. Zhou, C. Xia, X. Shan, and Z. Yang, "The impact of bogie sections on the wake dynamics of a high-speed train," Flow, Turbulence and Combustion (2019).

[35]N. Ashton, A. West, S. Lardeau, and A. Revell, "Assessment of RANS and DES methods for realistic automotive models," Computers Fluids **128** (2016).

[36]M. Gritskevich, A. Garbaruk, J. Schütze, and F. Menter, "Development of ddes and iddes formulations for the k-$\omega$ shear stress transport model," Flow, Turbulence and Combustion **88** (2012).

[37]P. Spalart, "Detached-eddy simulation," Annual Review of Fluid Mechanics **41**, 181–202 (2009).

[38]M. Shur, P. Spalart, M. Strelets, and A. Travin, "A hybrid rans-les approach with delayed-des and wall-modelled les capabilities," International Journal of Heat and Fluid Flow **29**, 1638–1649 (2008).

[39]N. Jarrin, S. Benhamadouche, D. Laurence, and R. Prosser, "A synthetic-eddy-method for generating inflow conditions for large-eddy simulation," International Journal of Heat and Fluid Flow **27**, 585–593 (2006).

[40]G. Bonnavion and O. Cadot, "Unstable wake dynamics of rectangular flat-backed bluff bodies with inclination and ground proximity," Journal of Fluid Mechanics **854**, 196–232 (2018).

[41]T. Wu, "Cavity and wake flows," Annual Review of Fluid Mechanics **4**, 243–284 (1972).

[42]M. Rouméas, P. Gilliéron, and A. Kourta, "Analysis and control of the near-wake flow over a squareback geometry," Computers & Fluids **38**, 60–70 (2009).

[43]G. Rigas, A. Morgans, R. D. Brackston, and J. Morrison, "Diffusive dynamics and stochastic models of turbulent axisymmetric wakes," Journal of Fluid Mechanics **778**, R2 (2015).

[44]B. Podvin, S. Pellerin, Y. Fraigneau, A. Evrard, and O. Cadot, "Proper orthogonal decomposition analysis and modelling of the wake deviation behind a squareback Ahmed body," Physical Review Fluids **5** (2020).

[45]Z. Wei, Z. Yang, C. Xia, and Q. Li, "Cluster-based reduced-order modeling of the wake stabilization mechanism behind a twisted cylinder," Journal of Wind Engineering and Industrial Aerodynamics **171** (2017).

[46]C. Xia, H. Wang, D. Bao, and Z. Yang, "Unsteady flow structures in the wake of a high-speed train," Experimental Thermal and Fluid Science **98** (2018).

[47]C. Xia, Z. Wei, H. Yuan, Q. Li, and Z. Yang, "Pod analysis of the wake behind a circular cylinder coated with porous media," Journal of Visualization (2018).

[48]B. Oudheusden, F. Scarano, N. Van Hinsberg, and D. Watt, "Phase-resolved characterization of vortex shedding in the near wake of a square-section cylinder at incidence," Experiments in Fluids **39**, 86–98 (2005).

[49]M. Legrand, J. Nogueira, and A. Lecuona, "Flow temporal reconstruction from non-time-

resolved data part i: Mathematic fundamentals," Experiments in Fluids **51**, 1047–1055 (2011).

[50]J. Gerrard, "The mechanics of the formation region of vortices behind bluff bodies," Journal of Fluid Mechanics **25**, 401–413 (1966).

[51]A. Evrard, O. Cadot, V. Herbert, D. Ricot, R. Vigneron, and J. Délery, "Fluid force and symmetry breaking modes of a 3D bluff body with a base cavity," Journal of Fluids and Structures **61**, 99–114 (2016).

[52]H.-J. Schmidt, R. Woszidlo, C. N. Nayeri, and C. O. Paschereit, "The effect of flow control on the wake dynamics of a rectangular bluff body in ground proximity," Experiments in Fluids **59**, 107 (2018).

[53]G. Pavia, M. Passmore, M. Varney, and G. Hodgson, "Salient three-dimensional features of the turbulent wake of a simplified square-back vehicle," Journal of Fluid Mechanics **888** (2020).

[54]R. D. Brackston, J. García De La Cruz, A. Wynn, G. Rigas, and J. F. Morrison, "Stochastic modelling and feedback control of bistability in a turbulent bluff body wake," Journal of Fluid Mechanics **802**, 726–749 (2016).

[55]H. Zhu, C.-Y. Wang, H.-P. Wang, and J. Wang, "Tomographic piv investigation on 3d wake structures for flow over a wall-mounted short cylinder," Journal of Fluid Mechanics **831**, 743–778 (2017).

[56]D. Barros, J. Borée, B. R. Noack, A. Spohn, and T. Ruiz, "Bluff body drag manipulation using pulsed jets and Coanda effect," Journal of Fluid Mechanics **805**, 422–459 (2016).